JGR Atmospheres

RESEARCH ARTICLE
10.1029/2020JD032686

Key Points:
- Vertical temperature gradients in a mountain valley range from −10°C km^{-1} to >60°C km^{-1} with strong diel and seasonal variability
- Cold-air pooling is the norm, and not the exception, in this landscape
- Synoptic-scale weather regulates nighttime inversions; topography and vegetation further regulate fine-scale daytime inversions

Supporting Information:
- Supporting Information S1

Correspondence to:
D. E. Rupp,
david.rupp@oregonstate.edu

Citation:
Rupp, D. E., Shafer, S. L., Daly, C., Jones, J. A., & Frey, S. J. K. (2020). Temperature gradients and inversions in a forested Cascade Range basin: Synoptic- to local-scale controls. *Journal of Geophysical Research: Atmospheres*, *125*, e2020JD032686. https://doi.org/10.1029/2020JD032686

Received 4 MAR 2020
Accepted 23 OCT 2020
Accepted article online 31 OCT 2020

Author Contributions:
Conceptualization: David E. Rupp, Sarah L. Shafer, Christopher Daly, Julia A. Jones
Data curation: David E. Rupp, Sarah J. K. Frey
Formal analysis: David E. Rupp
Funding acquisition: Sarah L. Shafer, Christopher Daly, Julia A. Jones
Investigation: David E. Rupp, Sarah L. Shafer, Christopher Daly, Julia A. Jones, Sarah J. K. Frey
Methodology: David E. Rupp, Sarah L. Shafer, Christopher Daly, Julia A. Jones
Project administration: Julia A. Jones
Resources: Christopher Daly
Visualization: David E. Rupp, Sarah J. K. Frey
Writing - original draft: David E. Rupp, Sarah L. Shafer
Writing – review & editing: David E. Rupp, Sarah L. Shafer, Christopher Daly, Julia A. Jones, Sarah J. K. Frey

Temperature Gradients and Inversions in a Forested Cascade Range Basin: Synoptic- to Local-Scale Controls

David E. Rupp[1], Sarah L. Shafer[2], Christopher Daly[3], Julia A. Jones[4], and Sarah J. K. Frey[4]

[1]Oregon Climate Change Research Institute, College of Earth, Ocean, and Atmospheric Sciences, Oregon State University, Corvallis, OR, USA, [2]U.S. Geological Survey, Corvallis, OR, USA, [3]PRISM Climate Group, Northwest Alliance for Computational Science and Engineering, College of Engineering, Oregon State University, Corvallis, OR, USA, [4]College of Earth, Ocean, and Atmospheric Sciences, Oregon State University, Corvallis, OR, USA

Abstract Cold-air pooling and associated air temperature inversions are important features of mountain landscapes, but incomplete understanding of their controlling factors hinders prediction of how they may mediate potential future climate changes at local scales. We evaluated how topographic and forest canopy effects on insolation and local winds altered the expression of synoptic-scale meteorological forcing on near-surface air temperature inversions and how these effects varied by time of day, season, and spatial scale. Using ~13 years of hourly temperature measurements in forest canopy openings and under the forest canopy at the H.J. Andrews Experimental Forest in the western Cascade Range of Oregon (USA), we calculated air temperature gradients at the basin scale (high vs. low elevation) and at the cross-valley scale for two transects that differed in topography and forest canopy cover. ERA5 and NCEP NCAR R1 reanalysis data were used to evaluate regional-scale conditions. Basin and cross-valley temperature inversions were frequent, particularly in winter and often persisted for several days. Nighttime inversions were more frequent at the cross-valley scale but displayed the same intra-annual pattern at the basin and regional scales, becoming most frequent in summer. Nighttime temperature gradients at basin and cross-valley scales responded similarly to regional-scale controls, particularly free-air temperature gradients, despite differences in topography and forest cover. In contrast, the intra-annual pattern of daytime inversions differed between the basin and cross-valley scales and between the two cross-valley transects, implying that topographic and canopy effects on insolation and local winds were key controls at these scales.

Plain Language Summary In mountains, the air is often colder at higher elevations than at lower elevations. However, under certain environmental conditions, cold air can pool in valleys, making the air colder at lower elevations than at higher elevations, creating an air temperature inversion. We used measurements of air temperature, sunlight, wind, and rain to understand how cold-air pools form, break up, and change throughout the day and from season to season in a forested basin in the Cascade Range of western Oregon (USA). We identified cold-air pools much more often in valleys ~1 to 2 km wide than previously estimated from basin-wide (~10-km scale) measurements. The seasonal variability of nighttime inversion frequency was similar at the basin and cross-valley scales, indicating that regional climate influences nighttime cold-air pooling at all scales. The seasonal variability of daytime inversion frequency was not the same across spatial scales, indicating that local factors, such as shading by steep valley walls, were important in the persistence of cold-air pools during the day. Understanding how and when cold-air pools form is important because they may be able to reduce the effects of potential future climate warming on plants and animals in mountain ecosystems.

1. Introduction

Cold-air pooling and associated temperature inversions are common in mountain landscapes (e.g., Miró et al., 2018; Novick et al., 2016; Whiteman et al., 2004), but gaps in our understanding of the relative importance of synoptic-scale and local factors on cold-air pool formation and breakup hinders efforts to predict how regional-scale climate variability and change may affect cold-air pooling (Zardi & Whiteman, 2013). It has been suggested that cold-air pooling would help mitigate the effects of projected future climate

changes experienced by some species and ecosystems, particularly in mountain regions (Curtis et al., 2014; Dobrowski, 2011; Lenoir et al., 2017; Novick et al., 2016). However, the extent of such mitigation would depend not only on the interactions between local cold-air pooling processes and synoptic and free-air atmospheric conditions but also on the interactions between the cold-air pools and the local processes that modify the expression of air temperatures at the land surface.

A cold-air pool is defined as the presence of air in a valley or depression that is colder than what would be expected relative to the temperature of the air above it, based on a reference rate at which air temperature, T_a, changes with elevation, z. In other words, the measured vertical temperature gradient Γ_a ($= \mathrm{d}T_a/\mathrm{d}z$) is greater than a reference temperature gradient, $\overline{\Gamma}_a$. (The temperature gradient is of opposite sign than the "lapse rate" ($-\mathrm{d}T_a/\mathrm{d}z$) used in meteorology that refers to the rate of decrease in air temperature with altitude.) Cold-air pooling can result in $\Gamma_a > 0$, a state known as a temperature inversion. A temperature inversion is frequently used to identify the presence of a cold-air pool, sometimes in conjunction with wind speeds below a threshold value (e.g., Reeves & Stensrud, 2009; Whiteman et al., 2001).

Cold-air pools form in multiple ways. One way is through local radiative imbalances: Drainage of cold air down a sloped surface develops when a net positive upward radiative flux at the surface initiates cooling of near-surface air (Marvin, 1914; Zardi & Whiteman, 2013). If this cooling air consequently achieves a density greater than that of the air farther from the surface but at the same altitude, the near-surface air will move downslope. Warmer air replaces the displaced air, subsequently cools, and itself drains. The draining air may continue downslope until reaching a surface barrier, constriction, or depression, or it may overlie previously drained air, forming a cold-air pool. Clear skies and the absence of insolation at night promote radiative cooling, while light winds and a stable atmosphere facilitate cold-air drainage (Barr & Orgill, 1989; Daly et al., 2010; Price et al., 2011).

Buoyancy-driven drainage is not the only way that cold-air pools initiate. They can develop at night in small valleys and undulations in terrain when sheltering decouples the air flow in the valley bottom from that aloft. Near the decoupled valley floor, the downward turbulent heat flux is reduced, allowing for more rapid radiative cooling there (e.g., Gustavsson et al., 1998; Vosper et al., 2014; Vosper & Brown, 2008). Cold-air pools can also form when air warms aloft but the processes governing the warming do not fully extend downward to the surface, preventing vertical mixing and resulting in little increase in near-surface air temperature. At the regional scale, warming at higher altitudes can occur by advection of warm air aloft, creating a stable layer in valleys that can persist for days, particularly during the winter (Arduini et al., 2020; Lareau et al., 2013; Reeves & Stensrud, 2009; Whiteman et al., 1999; Wolyn & McKee, 1989). At the local scale, cold-air pools can result from differential heating of a partially illuminated landscape, as may occur at low Sun angles (Zardi & Whiteman, 2013). Snow cover, with its high albedo, can also help maintain an existing cold-air pool by reducing surface warming during the day (Dorninger et al., 2011; Zängl, 2005).

A forest modulates the heat and radiative transfer within and below its canopy, which can lead to decoupling below and above canopy air flow (e.g., Belcher et al., 2012; Kiefer & Zhong, 2015). During the day as the canopy warms more than the ground surface, subcanopy inversions can form, driving cold-air drainage in the stable subcanopy, while thermally driven air flow above the canopy is upslope (Froelich & Schmid, 2006; Pypker, Unsworth, Lamb, et al., 2007; Staebler & Fitzjarrald, 2005; Tóta et al., 2012). After sunset, the cold-air drainage may weaken as the canopy cools faster than the surface, reducing the subcanopy stability (e.g., Mahrt et al., 2000; Whiteman, 1982). At night, sheltering provided by forests can also promote in situ cold-air pooling by reducing the downward turbulent heat flux (Gustavsson et al., 1998).

Although cold-air pooling is a common phenomenon in mountain landscapes, including in the Cascade Range of the western United States (Daly et al., 2010; Pypker, Unsworth, Lamb, et al., 2007; Ward et al., 2018), a long-term climatology of cold-air pooling is lacking for the Cascade Range, particularly below the forest canopy and at horizontal scales <10 km, as is a quantification of what controls the climatological pattern of cold-air pooling. In this study we use long-term (November 2005 to December 2018) subdaily meteorological data from the H.J. Andrews Experimental Forest (hereafter "Andrews Forest"), a steep, forested watershed in the Cascade Range of Oregon (USA), as well as regional reanalysis data, to investigate three basic properties of cold-air pooling at the basin and cross-valley scales: (1) how air temperature inversions, an index for cold-air pooling, vary throughout the day and year; (2) how these inversions vary with the location of measurement; and (3) the synoptic- and local-scale controls that drive the observed variability in

temperature gradients and inversions. Although this last topic has received much attention in general, much less is known about how synoptic weather patterns and local-scale factors (e.g., cloud cover) affect temperature gradients as measured below forest canopies in particular.

Numerous studies have used local near-surface air temperature gradients to investigate cold-air pooling dynamics, with analyses ranging from regional (>100 km) to fine (<1 km) spatial scales and seasonal to subhourly temporal scales. Studies focused on regional scales have often relied on data from existing meteorological stations (Dobrowski et al., 2009; Reeves & Stensrud, 2009), which may not be ideally placed for measuring cold-air pooling. Other studies have analyzed data collected over short distances (<10 km) but frequently over relatively short time periods: a couple of days (Kelsey et al., 2019), one or two seasons (Lareau et al., 2013; Pagès et al., 2017; Vitasse et al., 2017), one to a few years (Fridley, 2009; Jemmett-Smith et al., 2018; Joly & Richard, 2019; Miró et al., 2018; Pike et al., 2013; Reeves & Stensrud, 2009), and, rarely, as much as a decade (Whiteman et al., 2001). Our data set is unique, however, in its combination of a long temperature record (spanning 13 years and 2 months) with high spatial resolution (~0.14-km average spacing along two transects). Moreover, nearly all of the temperature data are from sensors placed beneath the canopy of a forest, which is the predominant vegetation in temperate montane regions.

2. Study Area and Data

2.1. Study Area

The Andrews Forest is a 64-km^2 steep, forested, westward draining watershed in the western Cascade Range that forms the eastern boundary of the Willamette Valley (122.26°W, 44.21°N; Figure 1 and supporting information Figure S1a). Elevation ranges from 430 to >1,600 m, and slopes are steep (>60% based on a 30-m horizontal resolution digital elevation model) over much of the site. Vegetation is dominated by Douglas-fir (*Pseudotsuga menziesii*) and western hemlock (*Tsuga heterophylla*) forest up to ~500 years of age and ranging from ~60 to >90 m in height. Slightly more than 25% of the watershed was clear-cut from 1948 to the early 1980s, and these sites were replanted or regenerated with Douglas-fir, producing stands with canopy heights today of <20 m.

The Andrews Forest has a Mediterranean climate characterized by relatively wet winters and dry summers. Approximately 75% of the annual precipitation falls during the months of November to April. Winter storm systems typically arrive from the southwest. Winter outbreaks of cold air from Canada are normally blocked by the crest of the Cascade Range and rarely affect the Andrews Forest. Winter air temperature is mild; the long-term mean of the January daily temperature minimum is −1.3°C and −2.5°C at 430 and 1,294 m, respectively. Snow is rare below 500 m, but a substantial snowpack typically accumulates above 900 m and persists from late November to June (Daly et al., 2010). In summer, high pressure over the northeastern Pacific Ocean dominates the climate, characterized by extended periods of clear, calm weather (Mock, 1996). The long-term mean of the July daily temperature maxima is 28.6°C and 22.1°C at 430 and 1,294 m, respectively, moderated by afternoon onshore flow from the Pacific Ocean (Daly et al., 2010).

2.2. Reanalysis Data

Gridded (0.25° × 0.25° horizontal resolution), hourly air temperature and geopotential height data at 25-hPa intervals in the lower troposphere were obtained from the European Centre for Medium-Range Weather Forecasts (ECMWF) Re-Analysis 5 data set (ERA5; Hersbach et al., 2020). Gridded (2.5° × 2.5° horizontal resolution), 6-hourly (6, 12, 18, and 24 UTC) geopotential height data at 700 hPa were obtained from the National Centers for Environmental Prediction–National Center for Atmospheric Research Reanalysis 1 data set (NCEP NCAR R1; Kalnay et al., 1996).

2.3. Andrews Forest Data

Near-surface air temperature (°C) data for this study were obtained from three Andrews Forest temperature sensor networks: meteorological stations, reference stands, and cold-air drainage transects (Figure 1 and Table 1).

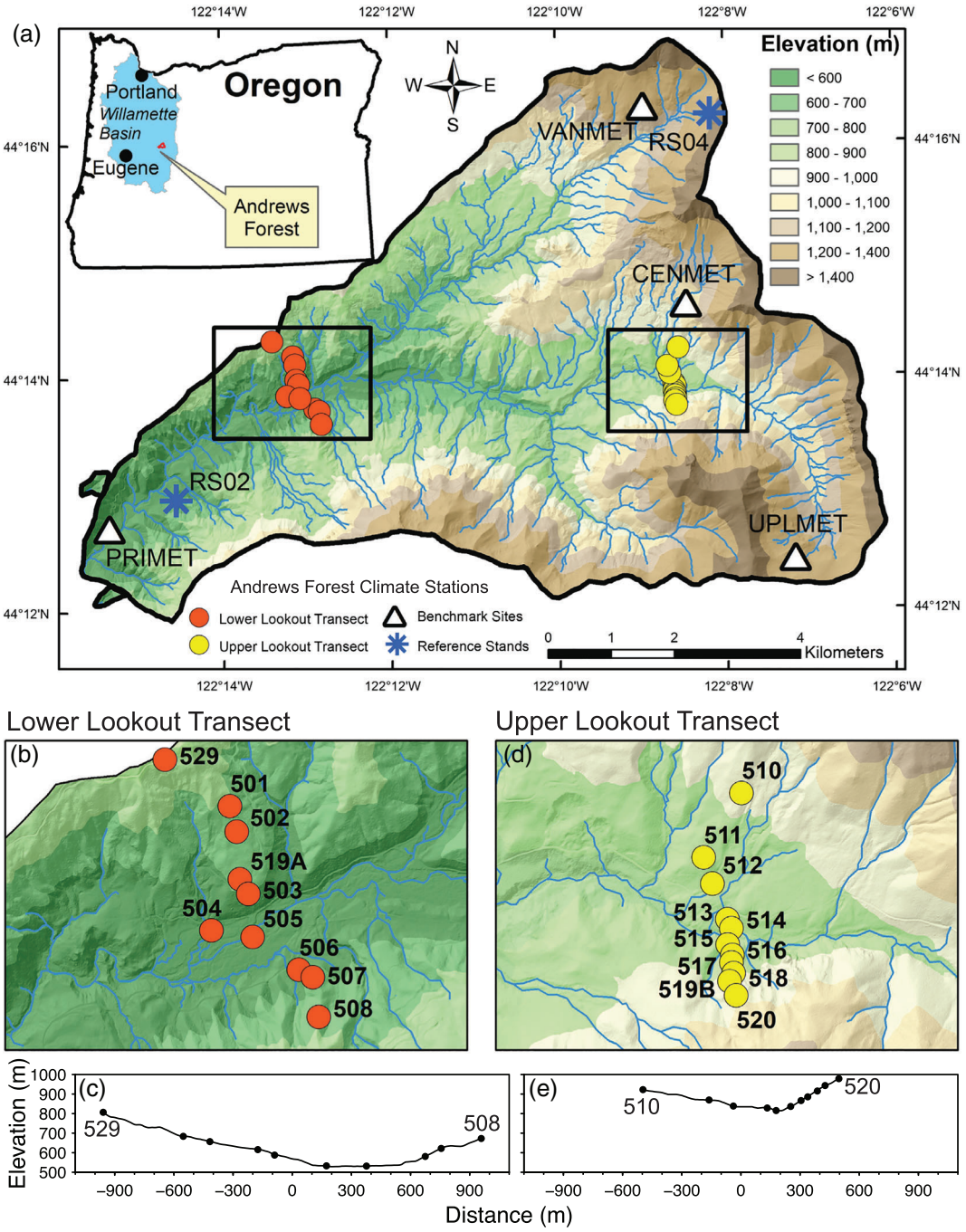

Figure 1. (a) Temperature sensor locations in Andrews Forest (HJA). Lower Lookout transect (b) sensor locations (red circles) and (c) transect elevation profile. Upper Lookout transect (d) sensor locations (yellow circles) and (e) transect elevation profile. Black circles in (c) and (e) indicate sensor locations along each transect.

2.3.1. Meteorological Station Data

Air temperature measurements at meteorological stations in forest clearings (mainly clear-cuts) began at the Andrews Forest in 1958, and five additional sites were initiated in the period 1972 to 1995 (Daly & McKee, 2019). We used hourly mean data from two meteorological stations to represent lower and upper elevations of the study area: the Primary meteorological station (PRIMET), located at an elevation of 436 m on a valley terrace (slope = 0°) in a 50-m diameter clearing, and the Vanilla Leaf meteorological station (VANMET), located at 1,268-m elevation in a 25 × 30-m clearing on a south facing slope

Table 1
Summary of Near Surface Air Temperature Measurements Used in This Study

Property	Meteorological stations (MET)	Reference stands (RS)	Cold-air drainage transects (LLT and ULT)
Sensor identifiers	VANMET, PRIMET	RS04, RS02	LLT: 501–508, 519A, 529 ULT: 510–518, 519B,520[a]
Number of stations	2	2	21
Finest temporal resolution	5 min[b]	5 min[c]	15 min
Period of record used[d]	November 2005–December 2018	November 2005 to December 2018	November 2005 to December 2018
Elevation range (m)	436–1,268	490–1,310	LLT: 532–807 ULT: 816–979
Elevation gradient (%)	8	8	LLT north facing: 14 LLT south facing: 13 ULT north facing: 31 ULT south facing: 9
Andrews Forest database ID	MS001	MS005	MS036

Note. All measurements were taken at ~1.5-m above surface, with the exception of some measurements at the MET stations, where sensors at heights above 1.5 m were used to replace measurements that were missing or believed to be errors. LLT = Lower Lookout transect; ULT = Upper Lookout transect.
[a]There are two 519 stations: 519A and 519B. [b]Prior to 15 May 2014, resolution was 15 min for PRIMET; Prior to 21 May 2014, resolution was 15 min for VANMET. [c]Prior to 9 April 2014, resolution was 60 min for RS02; Prior to 29 May 2014, resolution was 60 min for VANMET. [d]The MET and RS records start before November 2005, but we used data from November 2005 to match the years of the LLT and ULT records.

(slope = 13°, aspect = 180°) (Figure 1 and supporting information Figures S1b and S1c; Daly & McKee, 2019). PRIMET and VANMET are approximately 10 km apart.

2.3.2. Reference Stand Data

Subcanopy (1.5-m) air temperature measurements from a network of old-growth forest "reference" stands began at the Andrews Forest in the early 1970s (Daly & McKee, 2016; Zobel et al., 1976). We used hourly mean data from two reference stand stations near PRIMET and VANMET to represent lower and upper elevations under the forest canopy: Reference Stand 2 (RS02, supporting information Figure S1d), located in a valley at an elevation of 490 m on a northwest facing slope (slope = 22°, aspect = 285°) with ~77% canopy cover, and Reference Stand 4 (RS04), located near a ridge top at an elevation of 1,310 m on a west facing slope (slope = 27°, aspect = 270°; Figure 1) with ~81% canopy cover.

2.3.3. Cold-Air Drainage Transect Data

A set of cross-valley transects were established in July 2002 specifically for investigating cold-air drainage and pooling in the Lookout Creek valley (Daly, 2017). We used data from the Lower Lookout transect (hereafter lower transect; ~2 km long with 10 sensors) and the Upper Lookout transect (hereafter upper transect; ~1 km long with 11 sensors) (Figure 1 and Table 1). Beginning near the end of October 2005, temperature and illumination were recorded concurrently at each location. We used data from 1 November 2005 through 31 December 2018. Each transect has an approximately north facing side and a south facing side (Figure 1 and Table 1). Compared to the lower transect, the upper transect crosses a narrower valley and has a taller and denser forest canopy along the valley floor.

At the lower and upper transect sites, instantaneous air temperature and illumination were measured at 15-min intervals with an Onset HOBO sensor and datalogger mounted on rebar approximately 1.5 m above the ground surface (supporting information Figures S1e and S1f). These naturally aspirated sensors are suspended under radiation shields made of PVC pipe but nevertheless can record a higher temperature than can a fan-aspirated sensor when the shield is in direct sunlight (Malek, 2019; Nakamura & Mahrt, 2005). We applied an adjustment to the measured temperature data, based on paired measurements of fan-aspirated and naturally aspirated temperature, T (°C), using a linear function of light, L (lux), within the radiation shield to get an adjusted temperature, $T_{adj} = T - (0.0002267L + 0.04955)$ (coefficients updated from Malek, 2019, for this study). The data used to derive the above equation excluded times when the wind speed measured alongside the paired sensors was greater than 0.5 m s^{-1}, to better reflect low-wind conditions representative of the subcanopy, particularly in summer when wind speeds are lowest and illumination tends to be highest. We excluded temperature data that had corresponding light values ≥20,000 lux from all statistical analyses, because 20,000 lux was the upper limit of L used when developing the adjustment equation. A value above 20,000 lux could also indicate a sensor had received a large amount of sunlight reflected off surfaces, including snow cover. This 20,000 lux upper limit capped the temperature

adjustment at −4.58°C. The median adjustment for all sensors was −0.19°C, while the two sensors receiving the most direct sunlight, 518 and 520, had median adjustments of −0.34°C. Across the sensors, the adjustment exceeded −2°C from 0% (e.g., sensors 507 and 508) to 4.9% (e.g., sensor 518) of daytime measurements. (See supporting information section S1 for examples of time series illustrating the effect of the adjustment.)

We flagged transect temperature data, prior to temperature adjustment, that did not meet automated quality control criteria (supporting information Table S1) or appeared unrealistically anomalous by manual visual inspection (Daly, 2017). These flagged data were excluded from our analyses (7% of all observations). Both the 15-min raw and adjusted data meeting quality control criteria were averaged to hourly intervals.

2.3.4. Other Data

We used additional Andrews Forest data sets (Daly & McKee, 2019) to examine relationships between other local weather variables and vertical temperature gradients. Wind velocity (m s^{-1}) at a height of 10 m was measured with a mechanical wind monitor at the Central meteorological station (CENMET), PRIMET, the Upper Lookout meteorological station (UPLMET), and VANMET, which are all in large clearings but at different elevations and topographic positions (Figure 1). We estimated Andrews Forest precipitation (mm h^{-1}) using a multisite mean of PRIMET, CENMET, and UPLMET data. Insolation (W m^{-2}) was measured by a pyranometer at VANMET and PRIMET. Snow depth (mm) was measured daily (local midnight) with a sonic ranging sensor at VANMET. The VANMET site was considered to be largely snow covered if the measured snow depth was 5 cm or more (e.g., Stevens, 2010). Snow depth was not measured at PRIMET because persistent snow cover there is uncommon.

3. Methods

3.1. Reanalysis Temperature Gradients and Synoptic-Scale Circulation Indices

Vertical air temperature gradients, Γ_a, across several altitude ranges were calculated from the ERA5 temperatures and geopotential heights for a grid cell ~65 km west of the Andrews Forest (123.00°W, 44.25°N). This grid cell is in the Willamette Valley and was chosen because it was the nearest grid cell in the ERA5 data whose surface elevation (257 m) was well below the minimum elevation of our site (436 m). After interpolating hourly ERA5 temperatures at the varying geopotential heights to fixed altitudes, we calculated temperature gradients between altitudes corresponding to the elevations of the following pairs of sensors: PRIMET, VANMET; RS02, RS04; 505, 529 (lower transect); and 514, 520 (upper transect). While the lowest altitude (436 m) was likely above the surface boundary layer nearly all of the time, under some conditions the lower geopotential height used for the calculations likely lay within the surface boundary layer. However, to distinguish the ERA5 temperature gradients from those based on near-surface measurements (section 3.2), we refer to ERA5 temperature gradients as "free-air" gradients.

Circulation indices of geostrophic flow strength and curvature (vorticity) were derived from the NCEP NCAR R1 700-hPa geopotential heights using the algorithm in Losleben et al. (2000) adapted for midlatitudes from the method of Jenkinson and Collison (1977). Geopotential heights were linearly interpolated to an hourly time step prior to calculating the indices. The algorithm calculates southerly and westerly flow strength indices, which are combined into a total flow strength index (F), and southerly and westerly vorticity components, which are combined into total vorticity of the flow (V). To characterize weather at the synoptic scale, the algorithm uses a 5 × 5 array of grid points at a 5° × 5° horizontal resolution (i.e., skipping every other grid point on the NCEP NCAR R1 2.5° × 2.5° grid). Following Daly et al. (2010), each time step was assigned to an anticyclonic (A), zonal (Z; weak curvature relative to flow strength), or cyclonic (C) category based on the sign of V and a comparison of the magnitudes of V and F. The array was centered on the grid cell closest to the Andrews Forest (122.5°W, 45°N; approximately 90 km from the Andrews Forest). Daly et al. (2010) found that the indices calculated for this location and at 700 hPa explained a large amount of the variance in daily temperature at PRIMET and VANMET.

3.2. Local Vertical Temperature Gradients, Cold-Air Pooling Identification, and a Cloudiness Index

We calculated local vertical temperature gradients using horizontally spaced near-surface observations. We refer to these gradients simply as "temperature gradients" throughout the rest of this paper and represent

them with the symbol Γ_s (s for surface). We calculated Γ_s in two ways. From the meteorological station (PRIMET and VANMET) and reference stand (RS02 and RS04) data, Γ_s was calculated as the difference in the temperature (°C) at the higher-elevation site minus the temperature at the lower-elevation site (VANMET minus PRIMET; RS04 minus RS02) divided by their elevation difference (km). For the lower and upper transects, Γ_s was calculated using a linear regression of adjusted temperature (see section 2.3.3) on elevation (lower: 501–508, 519A, and 529; upper: 510–518, 519B, and 520; see Figure 1 for site locations). Transect temperature gradients were only calculated when at least eight sensors on a transect had values that met the quality criteria (see section 2.3.3). Transect temperature gradients were excluded from analyses when regression residuals were very large, i.e., the root mean square error was >50°C. This removed the most extreme gradients (those of hundreds of °C km^{-1} and greater) but had negligible impact on the statistics calculated in this study.

Gradients from VANMET-PRIMET and RS04-RS02 represented basin-scale variability (i.e., from high to low elevations in the basin), while gradients at the lower and upper transects represented the local landform-scale (i.e., cross-valley) variability. Gradients at RS04-RS02 and the lower and upper transects were based on temperature measured under the forest canopy, whereas gradients at VANMET-PRIMET were based on temperature measured in canopy openings; gradients at the lower transect were from a relatively wide valley (~2 km), while those at the upper transect were from a narrow valley (~1 km).

We defined a cold-air pool to be present when Γ_s indicated a temperature inversion >0°C km^{-1} (Whiteman et al., 2001). Climatological mean inversion frequency was calculated for each hour of the day and each month of the year. Confidence intervals on the mean inversion frequencies were calculated with the Clopper-Pearson interval using the "binom" package in R (Dorai-Raj, 2014). Persistent cold-air pools were defined as uninterrupted, positive mean hourly temperature gradients (inversions) lasting at least 18 h (Whiteman et al., 2001). Although wind speed thresholds have been used as a second criterion for identifying cold-air pools, wind speed data were not available for the reference stands or transects. Andrews Forest nocturnal wind speeds near the ground surface are typically low, e.g., <1.5 m s^{-1} for May–December (Pypker, Unsworth, Mix, et al., 2007), and less than wind speed thresholds used in other studies (e.g., Whiteman et al., 2001).

A daily cloud cover index was used to examine the relationship of temperature inversions with cloudiness. The cloud cover index was calculated from the ratio of daily observed insolation to clear-sky insolation at VANMET, where clear-sky insolation was estimated using the R "insol" package (Corripio, 2019; see supporting information section S2). The index ranges from 0 (clear sky) to 1 (maximum overcast conditions), and a single index value was applied for midnight to midnight each day.

3.3. Environmental Influences on Temperature Gradients

We fitted multivariate linear regression models to quantify the effects of environmental factors on measured hourly mean air temperature gradients at 06:00 PST and 14:00 PST, separately, at the basin scale (VANMET-PRIMET and RS04-RS02) and valley cross-section scale (lower and upper transects). These two hours were chosen to represent times of high and low inversion frequency. At ~06:00 PST, cold-air pools were often near their deepest before solar heating became a factor on the valley floor. At ~14:00 PST, the effect of solar heating and mixing down to the valley floor was typically strongest. Predictor variables included vorticity index and flow strength index calculated from NCEP NCAR R1, free-air temperature gradient from ERA5, daily clear-sky insolation, and daily cloudiness index. The data derived from NCEP NCAR R1 and ERA5 were at the same hours as the local temperature gradients (06:00 PST and 14:00 PST). Hourly presence/absence of precipitation was originally considered but was discarded because of its high correlation ($r = 0.7$) with cloudiness. We assessed the contribution of each predictor variable to fitted multivariate models based on its relative importance, i.e., its proportionate contribution to R^2 individually and combined with other variables (Johnson & LeBreton, 2004), using the "relaimpo" package in R (Grömping, 2006). (We repeated the analysis with boosted regression trees (e.g., Elith et al., 2008) using the R "dismo" package (Hijmans et al., 2017), and the results were similar with respect to ranking of importance of predictors; see supporting information section S3 and Figure S2).

4. Results

4.1. Temperature Gradient Climatology

4.1.1. Diel Patterns in Temperature Inversions

The frequency of temperature inversions varied by time of day, month, and spatial scale of measurement (Figure 2). Basin-scale inversions based on differences between upper and lower elevation temperatures (i.e., VANMET-PRIMET and RS04-RS02) were more frequent at night and were rare on summer days. Inversions based on the upper and lower transect data loosely followed this general pattern (Figure 2) but were overall more frequent. Inversions at the lower transect, where the valley is broader (Figure 1), more closely matched the basin-scale patterns, although inversions at the lower transect tended to form earlier in the afternoon. In contrast, inversions at the upper transect, where the valley is narrower (Figure 1), persisted throughout much of the daytime and nighttime hours in all months (Figure 2). Basin-scale temperature inversions were generally less frequent throughout the day when calculated using temperatures measured beneath the forest canopy (RS04-RS02) than when using temperature measured in the clearings occupied by the meteorological stations (VANMET-PRIMET), and the southerly aspect of the upper-basin VANMET site may have also contributed to higher daytime inversion frequency using VANMET-PRIMET measurements. The conspicuous spike in VANMET-PRIMET inversions between 16:00 and 18:00 PST throughout the year is a result of PRIMET being more shaded from direct sunlight 2 to 3 h before VANMET (see supporting information Figure S3).

For the basin-scale measurements, there was an approximately 4-h delay in mean timing of inversion formation and breakup with respect to local sunset and sunrise times (estimated for an unobstructed horizontal surface). At the basin scale in spring and summer, the frequency of inversions increased gradually after sunset throughout the night, peaking after sunrise, whereas at the transects, the maximum inversion frequency was reached within roughly 4 h after sunset (Figure 2). Because of the ~4-h lag at the basin scale, we defined nighttime inversion periods as beginning 4 h after sunset and ending 4 h after sunrise. Daytime inversion periods were assigned the remaining hours (i.e., the time of sunrise plus 4 h to the time of sunset plus 4 h). Other studies have found similar time lags (i.e., ~3–5 h) in the formation and breakup of inversions relative to sunset and sunrise (De Wekker & Whiteman, 2006; Watanabe, 1994; Whiteman, 1982; Whiteman et al., 2004; Zardi & Whiteman, 2013). These “nighttime inversion” and “daytime inversion” periods (Figure 2) were analyzed separately.

4.1.2. Seasonal Patterns in Nighttime and Daytime Temperature Inversions

Nighttime inversion frequency at the Andrews Forest peaked twice during the year, once in winter (January) and once in summer (July–September), with inversions occurring least frequently in spring (March–June) (Figure 3c). The highest nighttime inversion frequency coincides with the period of least cloudiness (summer; Figure 3a). While this intra-annual pattern was displayed at all spatial scales of measurement (Figure 3c), nighttime inversions overall were most frequent at the upper and lower transect scale (>45% of hours even in the month with the lowest frequency). In general, local inversion frequencies followed the same intra-annual pattern as ERA5 inversion frequencies (which represents the larger Willamette Valley to the west), but with ERA5 having lower frequencies during three-quarters of the year (Figure 3e). From May through August, ERA5 inversion frequency roughly equaled or exceeded the Andrews Forest basin scale (VANMET-PRIMET and RS04-RS02) frequency. We speculate that the higher inversion frequencies in summer in ERA5 relative to the Andrews Forest at the basin scale is related to onshore surges of cool marine air that enter the Willamette Valley via low areas along the Oregon Coast Range (Cramer & Lynott, 1961; Dye et al., 2020; Mass et al., 1986) but whose influence wanes farther east up the valleys of the Cascade Range.

Daytime temperature inversions at the Andrews Forest were most frequent in winter (December–January), when clear-sky insolation was low (Figure 3b), and least frequent in spring (April–June), at all sites except at the upper transect (Figure 3d). We note that snow cover was often present in the uppermost part of the basin in spring, though it declined sharply after April (at VANMET, the fraction of days with snow cover dropped from 86% to 9% from April to June). Daytime inversions were frequent year-round at the upper and lower transect scale (~25% to 80% of hours), whereas inversion frequencies were low at the Andrews Forest basin scale from April to August (<10%). The ERA5 temperature gradients had a similar, though less pronounced, intra-annual pattern as the Andrews Forest basin-scale gradients (Figure 3f). Though ERA5 inversion frequencies were lower than Andrews Forest frequencies during most of the year, they equaled or exceeded

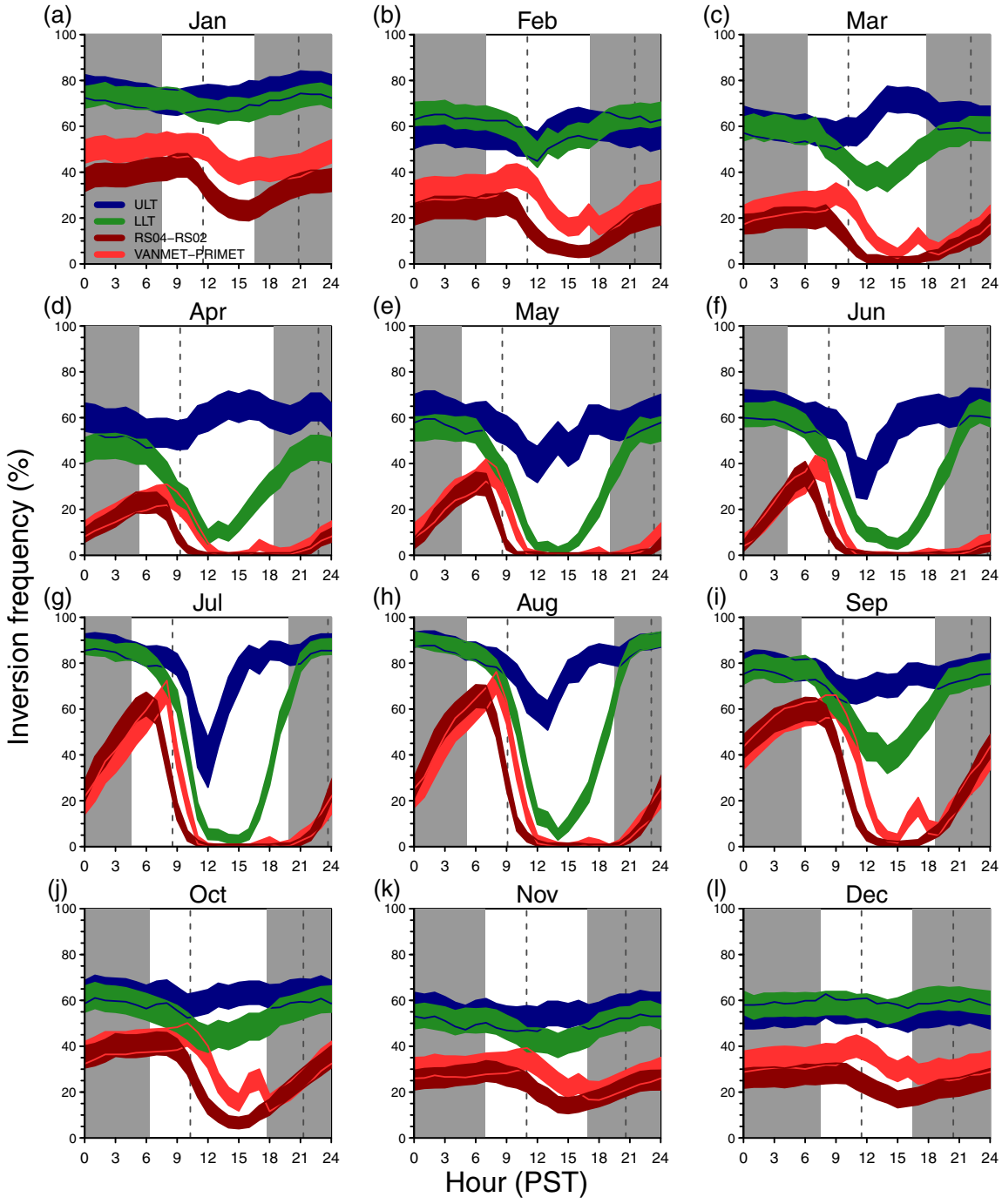

Figure 2. Variation in the frequency of hourly temperature inversions (November 2005 to December 2018) by time of day, month, and scale of measurement: VANMET-PRIMET (lighter red), RS04-RS02 (darker red), and the lower (LLT; green) and upper (ULT; blue) transects. The widths of the thick colored lines show the 95% confidence ranges of the frequency estimates (thin colored lines indicate the bottom or top of the confidence range where the thick colored lines overlap). Gray-shaded areas are nighttime (Sun below the horizon assuming flat terrain). Formation and breakup of inversions typically lag night-to-day and day-to-night transitions: The vertical dashed lines are offset 4 h from sunrise and sunset and separate the two periods of "nighttime inversions" and "daytime inversions" used in subsequent analyses.

Andrews Forest basin-scale frequencies in summer, which, as stated above, may be attributable to onshore surges of cool air into the Willamette Valley. The ERA5 inversion frequencies in summer were also notably higher at the heights of the ULT compared to the other heights. This may be because the ULT heights sample a layer of the atmosphere that is farther above the ground surface than the other layers sampled

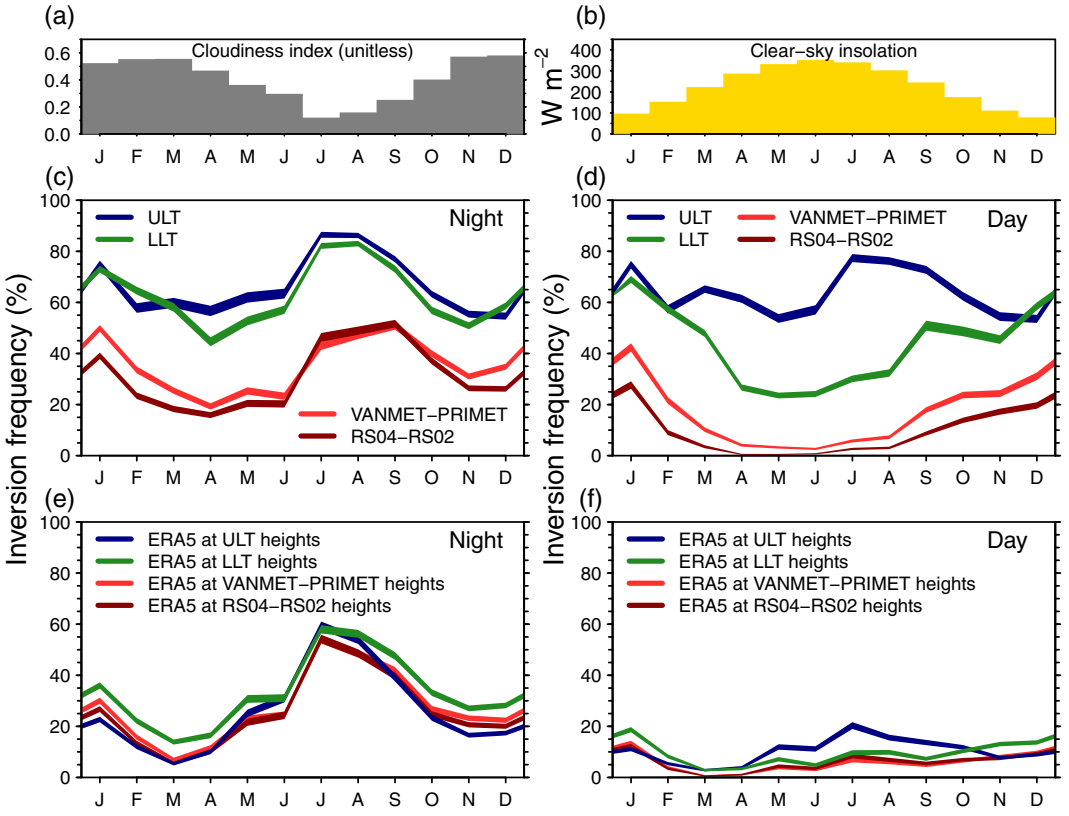

Figure 3. Variation in the mean monthly (a) cloudiness index and (b) clear-sky insolation at the Andrews Forest and variation in the frequency of (c, e) nighttime and (d, f) daytime hourly temperature inversions (November 2005 to December 2018) by month (c, d) at the Andrews Forest and (e, f) from ERA5 using the same heights as the Andrews Forest sensors but located over the southern Willamette Valley (~65 km due west of the Andrews Forest). Line thickness shows the 95% confidence range of the frequency estimates. LLT and ULT are the lower and upper transects, respectively.

(e.g., ERA5 at LLT heights). Because the daytime surface heating affects the lower heights more strongly, the heating is more likely to break up the ERA5 inversions measured across layers whose lower extent is closer to the surface.

It is worth commenting here on the impact of using illumination data paired with temperature data to reduce bias in the estimation of the valley-scale temperature gradients and inversions. The illumination-based filtering and temperature adjustment had the largest effect at the upper transect in summer, reducing the apparent daytime inversion frequency from 69% to 57% in June (the month with the largest effect), and over the entire year reduced the inversion frequency by 7%. On the lower transect, the change after the filtering and adjustment in inversion frequency was small and within ±1.2% in any month.

4.1.3. Seasonal Patterns in Persistent Temperature Inversions

The seasonal patterns of persistent temperature inversions (those which lasted for ≥18 h) generally followed the patterns of daytime inversion frequency (Table 2). The mean number and duration of persistent inversions was highest in winter (December–January) and as low as zero in spring and summer (April–August) except at the transects, where persistent inversions occurred in all months and tended to last longer. At the transects, the longest persistent inversion events occurred in December and January (>15 days), though very long events also occurred in summer at the upper transect (e.g., 13.4 days in one August).

4.1.4. Seasonal Patterns in Temperature Gradient Frequency Distributions

Nighttime temperature gradients at the lower and upper transects ranged from approximately −9.8°C km^{-1} (the dry adiabatic gradient) to values in excess of 60°C km^{-1} during most months of the year (60°C km^{-1} is equivalent to a temperature increase of >15°C from the bottom to the top of a transect; Figure 4). The shape of the frequency distributions varies seasonally but is always strongly positively skewed, so climatological mean values can be substantially greater than median values throughout the year.

Table 2
Characteristics of Persistent (≥18 h) Temperature Inversions by Month

	Mean number of persistent inversion episodes											
	Mean persistent inversion duration (days)											
	Maximum persistent inversion duration (days)											
Data source	Jan	Feb	Mar	Apr	May	Jun	Jul	Aug	Sep	Oct	Nov	Dec
ERA5 (1,310–490 m)	2.1	0.6	0.1	0.1	0.1	—	—	0.1	0.2	1.2	1.4	1.6
	1.9	*1.1*	*0.8*	*0.8*	*0.9*	—	—	*0.8*	*1.0*	*1.5*	*1.9*	*2.2*
	9.3	1.7	0.8	0.8	0.9	—	—	0.8	1.5	5.4	9.1	10.6
Meteorological stations (VANMET-PRIMET)	4.3	3.2	1.2	0.3	—	—	—	0.1	2.2	3.6	3.2	3.4
	2.6	*1.6*	*1.4*	*0.8*	—	—	—	*0.8*	*1.1*	*1.7*	*2.2*	*2.5*
	13.8	5.9	3.0	0.9	—	—	—	0.8	3.8	7.9	9.4	9.8
Reference stands (RS04-RS02)	3.8	1.6	0.9	—	—	—	—	—	1.0	3.2	2.6	2.4
	2.1	*1.4*	*1.0*	—	—	—	—	—	*1.0*	*1.2*	*2.0*	*2.6*
	11.8	4.5	1.7	—	—	—	—	—	3.8	2.8	6.8	8.7
Lower Lookout transect (LLT)	4.9	4.2	6.4	5.0	3.5	3.3	5.0	8.0	7.1	5.0	4.9	5.0
	3.9	*3.1*	*1.9*	*1.1*	*0.8*	*1.0*	*0.9*	*0.9*	*2.2*	*2.7*	*2.6*	*3.6*
	15.4	9.0	8.9	3.8	2.0	2.9	2.9	3.8	9.1	14.0	10.5	15.8
Upper Lookout transect (ULT)	4.7	4.4	6.3	6.7	9.9	12.6	14.9	16.3	5.3	6.2	5.2	4.9
	4.2	*3.0*	*2.8*	*1.9*	*1.1*	*0.9*	*0.9*	*1.3*	*3.5*	*2.7*	*2.9*	*3.1*
	15.2	10.5	13.6	6.9	7.0	2.1	2.9	13.4	11.6	12.3	10.8	11.8

Note. Persistent temperature gradient inversion episodes were assigned to the month in which they began.

Monthly median values were highest for August and September at both the lower (9.0°C km^{-1}) and upper (14.3°C km^{-1} and 14.0°C km^{-1}) transects. Median values were lowest for April at the lower transect (−1.2°C km^{-1}) but lowest for December at the upper transect (0.9°C km^{-1}). The distributions are generally unimodal for October through April and generally bimodal for May through September, indicating two dominant conditions: inversions (values >0°C km^{-1}) and well-mixed air with values approaching the standard environmental temperature gradient of −6.5°C km^{-1} (NOAA, 1976).

The general patterns of nighttime temperature gradients described above for the transects also apply to the Andrews Forest basin-scale temperature gradients (i.e., VANMET-PRIMET and RS04-RS02) in a relative sense, although the basin-scale gradients span a smaller range and the median and mean are lower than the transect gradients (Figure 5). Frequency distributions of nighttime gradients in ERA5 are remarkably similar to those at the basin scale, except that the upper range of values is reduced (Figure 6). At the basin and ERA5 scales, spring has the fewest positive gradients, indicating the prevalence of well-mixed conditions, even at night. Gradients at both scales show a mode near 0°C km^{-1} in summer that shifts to negative values in fall. The transition months of June and September have bimodal distributions.

Daytime temperature gradients at the transects also range from approximately the dry adiabatic gradient rate to values >60°C km^{-1} (Figure 7). The frequency distributions of the daytime temperature gradients are also strongly positively skewed. Monthly median values are highest for January at the lower transect (7.0°C km^{-1}) and for September at the upper transect (12.7°C km^{-1}). Median values are lowest for May at the lower transect (−6.0°C km^{-1}) and lowest for December (0.6°C km^{-1}) at the upper transect. Distributions are unimodal, with the exception of the lower transect in September. The mode of the distribution in most months approaches the standard environmental temperature gradient (−6.5°C km^{-1}) for both the upper and lower transects, although the mode at the upper transect is >0°C km^{-1} for July and August.

The general daytime patterns described above, especially for the lower transect, also apply to the basin-scale temperature gradients (Figure 8), although the basin-scale gradients have a smaller range than have the transect gradients and the basin-scale mean gradients are also lower. Daytime and nighttime gradients are similar in winter, showing a long tail of positive (inverted) values. In the higher Sun angle months of spring and summer, positive gradients are rare, although median and mean gradients are more negative in spring. Bimodal distributions are not evident in any month. Daytime patterns from ERA5 are similar to basin-scale

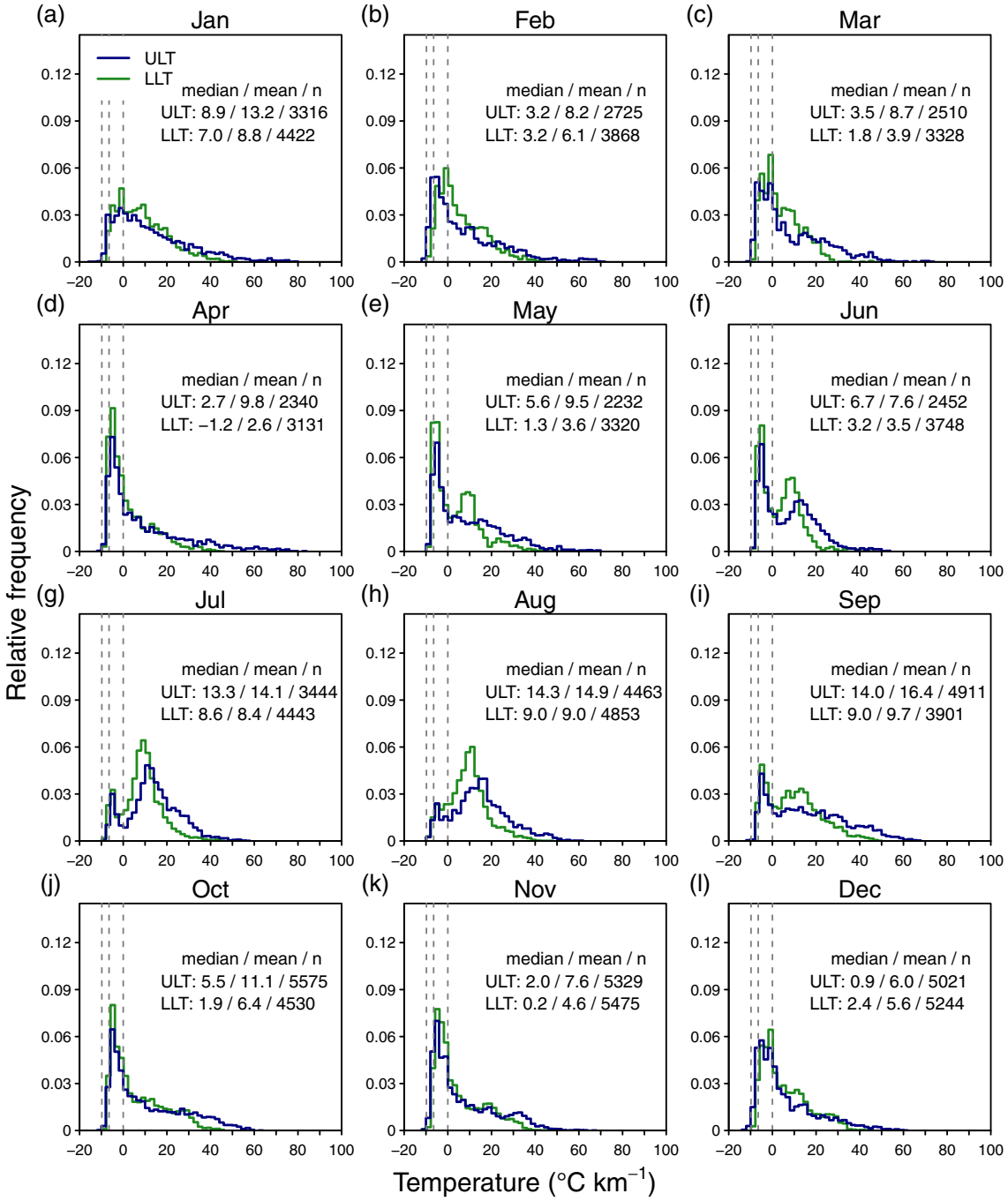

Figure 4. Frequency distribution of hourly nighttime temperature gradients (from 4 h past sunset to 4 h past sunrise; see Figure 2) for the period November 2005 through December 2018 at the lower (LLT, green line) and upper (ULT, blue line) transects. The values in each panel give the monthly median and mean hourly temperature gradient and sample size, *n*. The vertical dashed lines show the dry adiabatic gradient (−9.8°C km^{-1}), the environmental gradient (−6.5°C km^{-1}), and 0°C km^{-1}.

patterns (Figure 6, red lines), but the upper range in gradients is reduced in winter months, and ERA5 has a mode near the dry adiabatic gradient in summer that is not present in the basin-scale gradients (Figure 8).

4.2. Importance of Synoptic- to Local-Scale Controls on Temperature Gradients

Five environmental factors (ERA5 free-air temperature gradient, vorticity, flow strength, cloudiness, and clear-sky insolation) explain ~65% of the variance in magnitude of temperature gradients at 06:00 PST

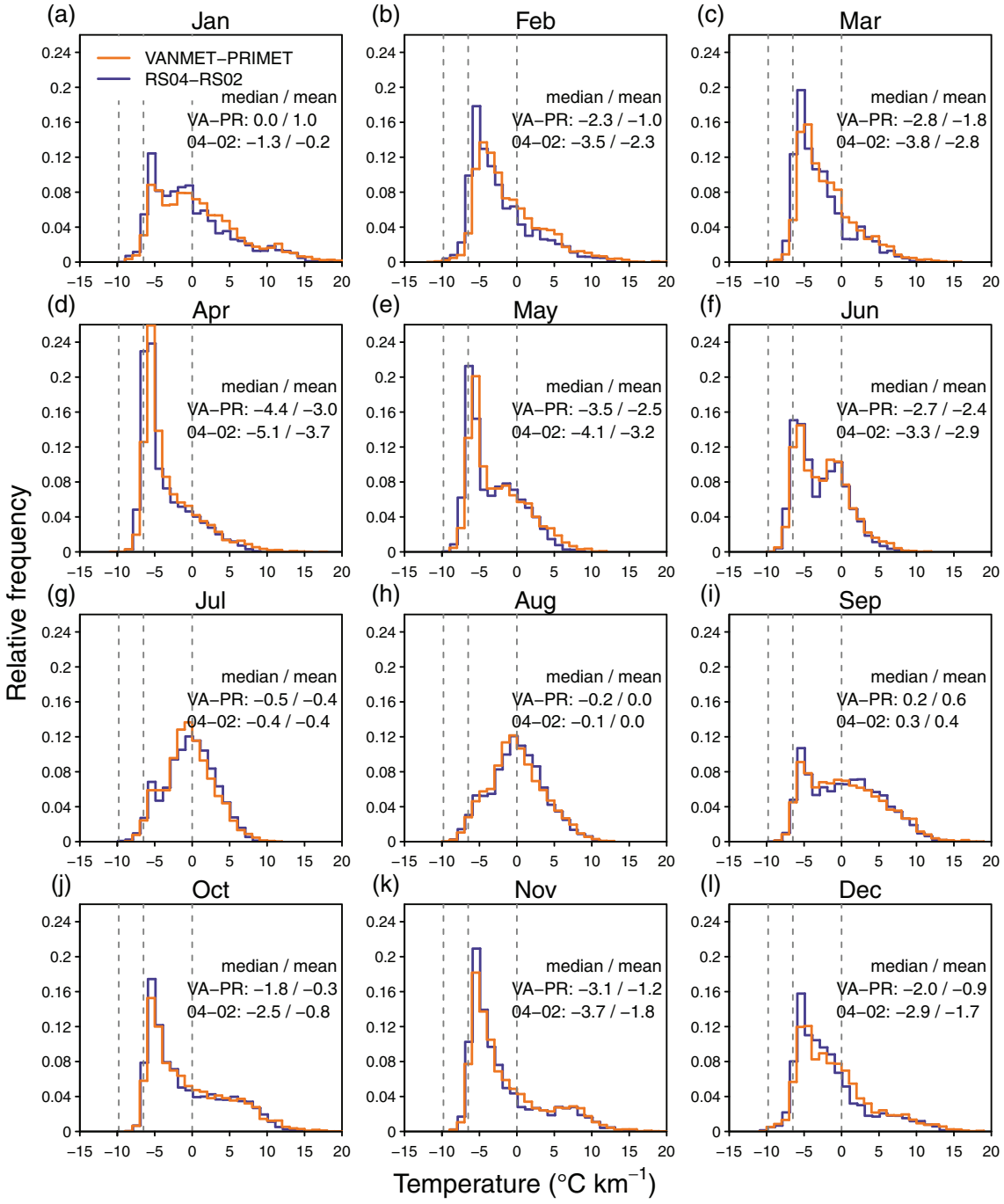

Figure 5. Frequency distribution of hourly nighttime temperature gradients (from 4 h past sunset to 4 h past sunrise; see Figure 2) for VANMET-PRIMET (VA-PR) and RS04-RS02 (04-02) for the period November 2005 through December 2018. The values in each panel give the monthly median and mean hourly temperature gradient. The vertical dashed lines show the dry adiabatic gradient (−9.8°C km^{-1}), the environmental gradient (−6.5°C km^{-1}), and 0°C km^{-1}.

(predawn or early morning, when gradients tend to be positive) at the basin scale and ~45% of the variance at the cross-valley scale (Figure 9a). The free-air temperature gradient is by far the most important explanatory variable in multivariate regression models at the basin and cross-valley scales. The free-air temperature gradient is positively related to basin and cross-valley temperature gradients (supporting information Table S2), implying that local inversions tend to be stronger when an inversion is present over the southern Willamette Valley. Vorticity is the second most important factor at the basin scale and the upper

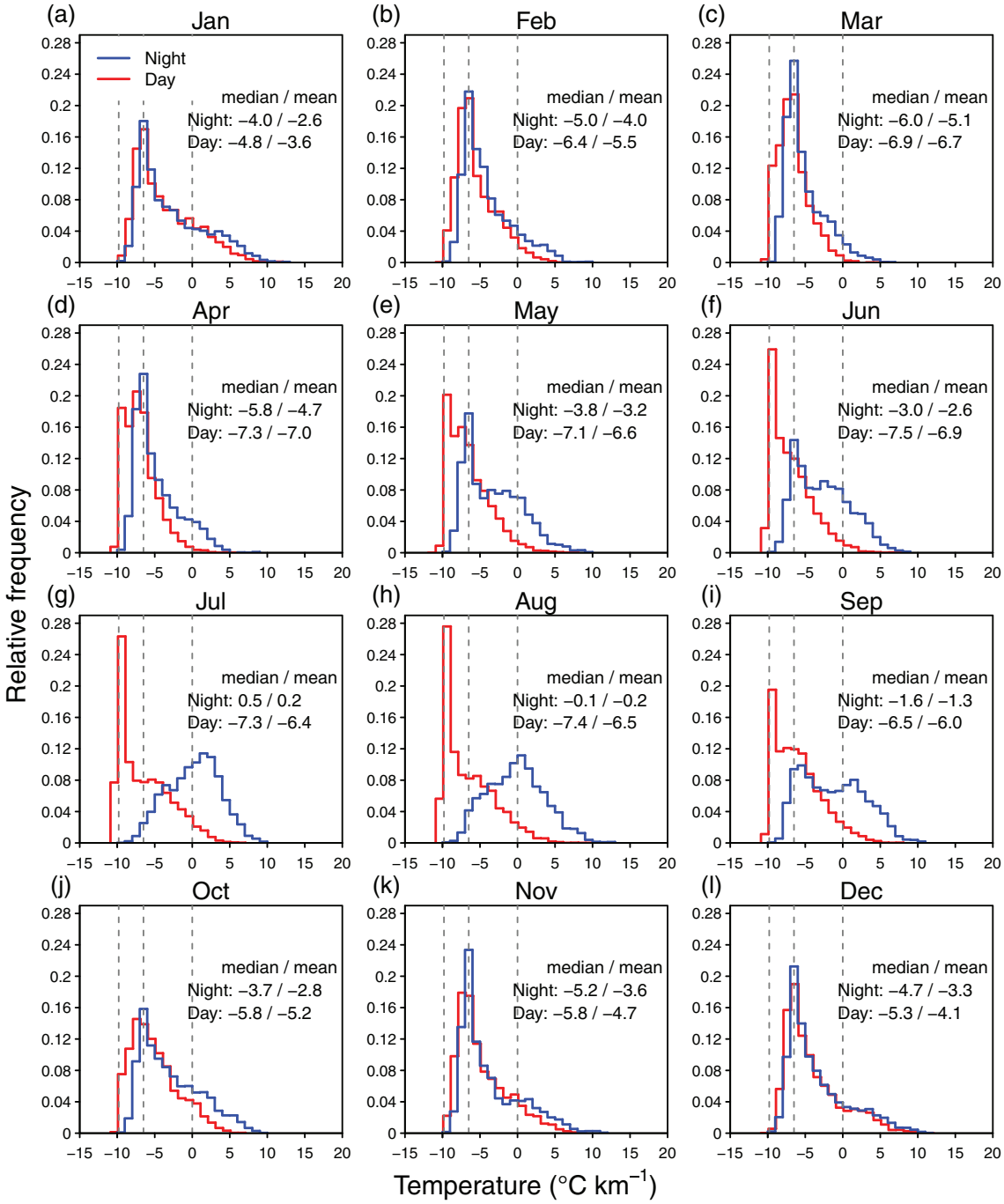

Figure 6. Frequency distribution of hourly nighttime (from 4 h past sunset to 4 h past sunrise) and daytime (from 4 h past sunrise to 4 h past sunset; see Figure 2) temperature gradients from ERA5 between the altitudes of 490 and 1,310 m (the same elevations as Andrews Forest sites RS02 and RS04, respectively) and approximately 65 km west of the Andrews Forest for the period November 2005 through December 2018. The values in each panel give the monthly median and mean hourly temperature gradient. The vertical dashed lines show the dry adiabatic gradient (−9.8°C km^{-1}), the environmental gradient (−6.5°C km^{-1}), and 0°C km^{-1}.

transect, and the negative coefficients (supporting information Table S2) imply that more positive vorticity (i.e., upward moving air) is associated with less positive/more negative temperature gradients, as expected. Cloudiness is the second most important factor for the lower transect and third most important for the other data sets, indicating that long-wave cooling plays a role in determining the temperature gradient; the negative regression coefficient (supporting information Table S2) implies that greater cloudiness is

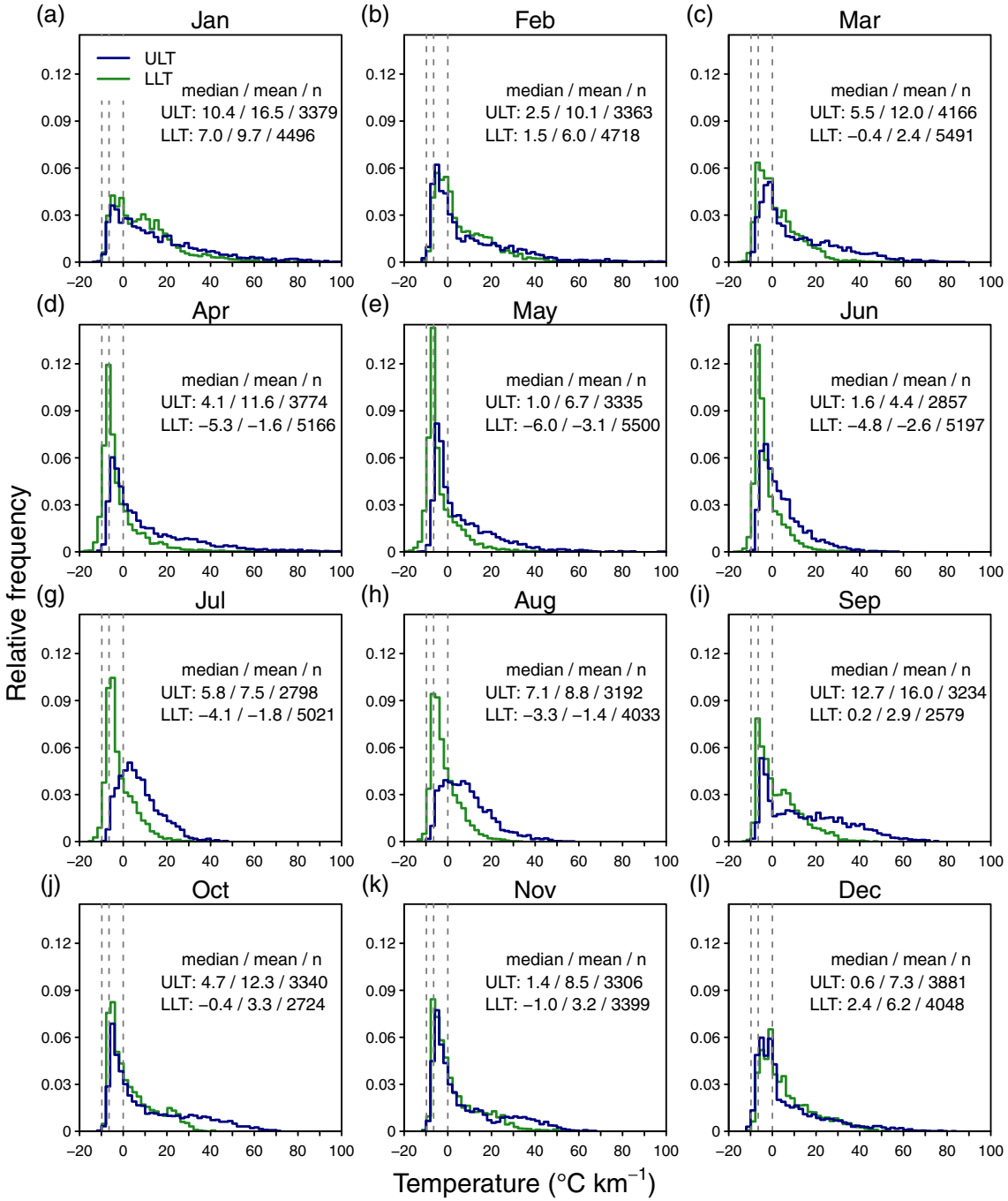

Figure 7. Frequency distribution of hourly daytime temperature gradients (from 4 h past sunrise to 4 h past sunset; see Figure 2) for November 2005 through December 2018 at the lower (LLT, green line) and upper (ULT, blue line) transects. The values in each panel give the monthly median and mean hourly temperature gradient and sample size, *n*. The vertical dashed lines show the dry adiabatic gradient (−9.8°C km^{-1}), the environmental gradient (−6.5°C km^{-1}), and 0°C km^{-1}.

associated with less positive/more negative gradients. The remaining factors (clear-sky insolation and flow strength) have little explanatory power.

In models of temperature gradients at 06:00 PST that exclude the free-air temperature gradient, vorticity and cloudiness are the most important explanatory variables, while the influence of clear-sky insolation and flow strength remain negligible (Figure 9c).

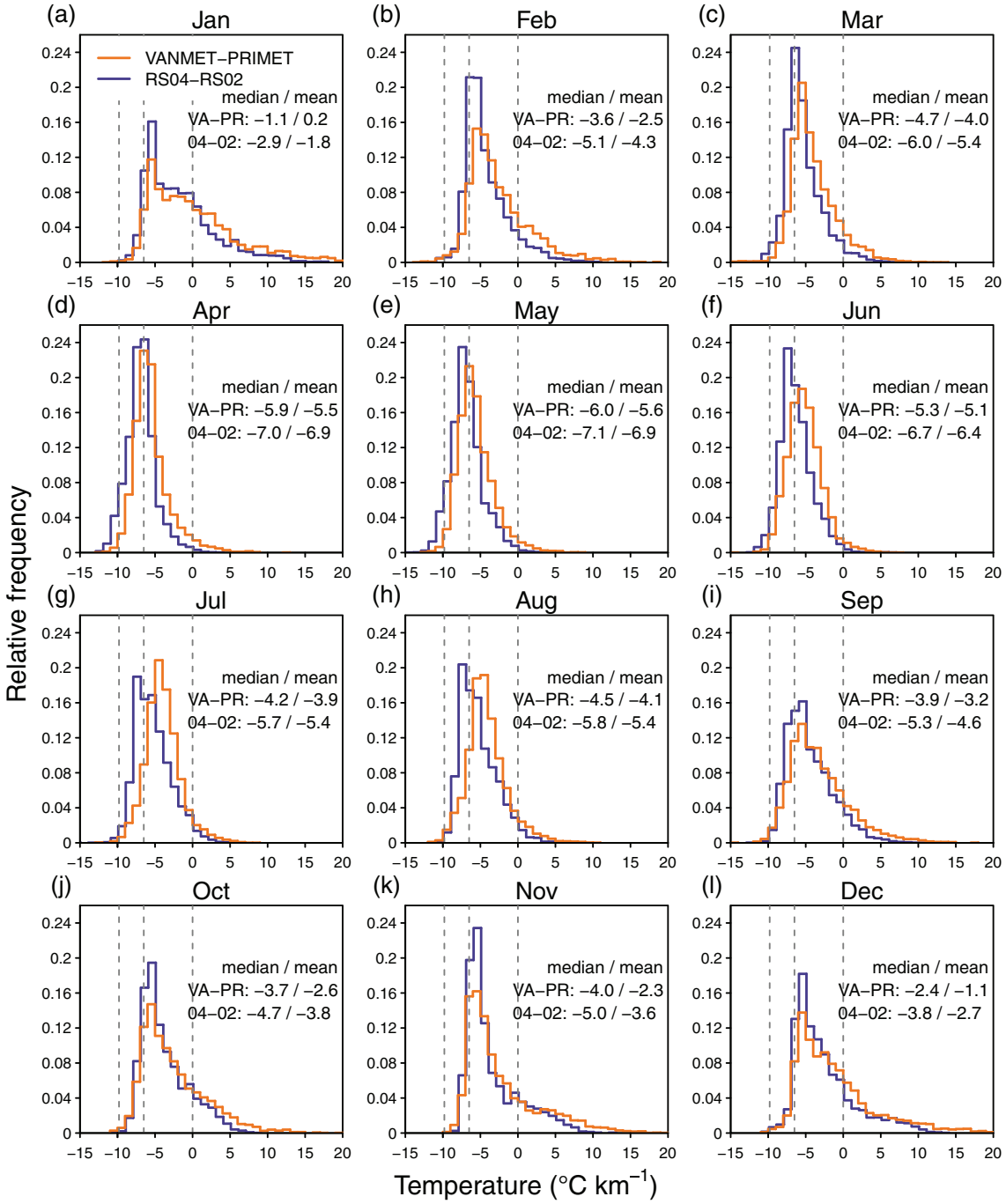

Figure 8. Frequency distribution of hourly daytime temperature gradients (from 4 h past sunrise to 4 h past sunset; see Figure 2) for VANMET-PRIMET (VA-PR) and RS04-RS02 (04-02) for the period November 2005 through December 2018. The values in each panel give the monthly median and mean hourly temperature gradient. The vertical dashed lines show the dry adiabatic gradient (−9.8°C km^{-1}), the environmental gradient (−6.5°C km^{-1}), and 0°C km^{-1}.

The same five environmental factors also explain approximately 65% and 50% of the variance in temperature gradients at 14:00 PST (early afternoon, when gradients tend to be negative) at the basin scale and the cross-valley scale, respectively (Figure 9b). Although the free-air temperature gradient is the most important factor at both scales, clear-sky insolation is the second most important factor at the basin scale and at the lower transect. The remaining variables explain relatively little variation except at the upper transect (a narrow valley), where vorticity and cloudiness are more important than clear-sky insolation.

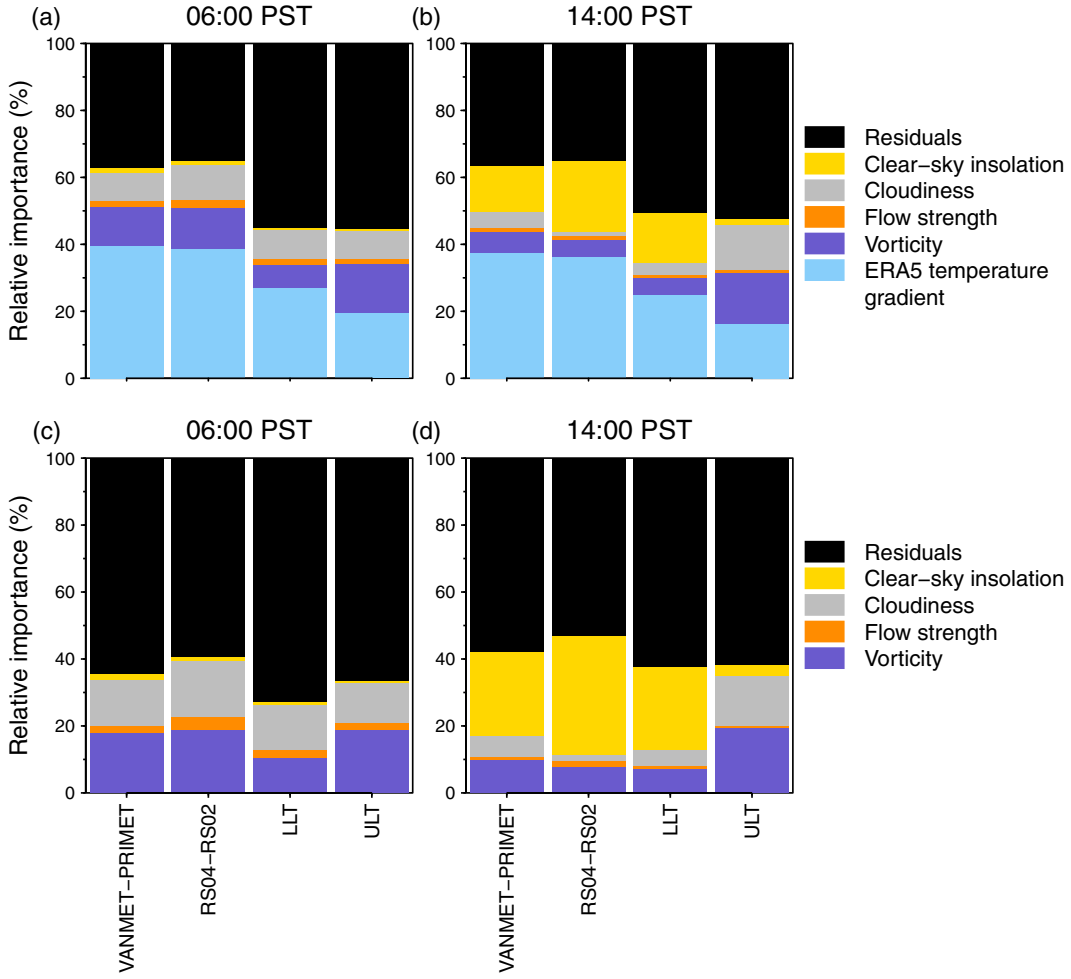

Figure 9. Relative contributions of environmental predictor variables in multivariate linear models for predicting the magnitude of temperature gradients at the basin scale (VANMET-PRIMET, RS04-RS02) and the cross-valley lower transect (LLT) and upper transect (ULT) scale at (a, c) 06:00 PST (nighttime) and (b, d)14:00 PST (daytime). Gradients at RS04-RS02, LLT, and ULT are based on temperature under the forest canopy, whereas gradients at VANMET-PRIMET are based on temperature in canopy openings. Gradients at LLT are in a wide valley (~2 km), whereas those at ULT are in a narrow valley (~1 km). The ERA5 temperature gradient was excluded from models in (c) and (d).

Excluding the free-air temperature gradient in models of Andrews Forest temperature gradients at 14:00 PST decreases the total variance explained by ~10–15%. Clear-sky insolation is by far the most important variable at the basin and cross-valley scales, except at the upper transect (Figure 9d), and is negatively related to inversion magnitude (supporting information Table S2), indicating that times of the year with more clear-sky radiation (i.e., spring and summer) have less positive/more negative daytime temperature gradients (Figure 3). At the upper transect, vorticity and cloudiness, in that order, are the most important factors (Figure 9d).

Multicollinearity of model variables can confound interpretation of regression results, and some of our environmental predictors are moderately correlated (supporting information Table S3). For example, cloudiness is generally higher when vorticity is higher, while clear-sky insolation is obviously higher in summer when flow strength and cloudiness tend to be low. Variance inflation factor scores greater than 5 or 10 (where a value of 1 indicates no collinearity) can help identify when collinearity is a problem. However, variance inflation factor scores for each variable were well below 5 (ranging from 1.4 to 2.2, depending on the model).

4.3. Case Studies: Nocturnal Summer and Persistent Winter Cold-Air Pooling

Our analysis documents two major and distinct types of air temperature inversions: (1) inversions produced by cold-air pools that form on summer nights and break up during the following daylight hours and (2) inversions produced by cold-air pools that form in winter and persist over multiple days. Here we describe in detail one example of each type of inversion as illustrations of the temporal development and breakup of such inversions and their connections to environmental conditions.

4.3.1. A Nocturnal Summer Cold-Air Pool

A particularly strong nighttime inversion formed during the night of 3 August 2012 when synoptic-scale conditions were favorable for cold-air drainage: A strongly inverted temperature profile developed over the southern Willamette Valley (Figure 10a) associated with weakly anticyclonic (clockwise) flow (negative vorticity) and weak winds aloft (implied by the widely spaced geopotential height contours in Figure 10b). The synoptic flow curvature classification was anticyclonic (A), indicating subsiding air. Locally, cloudless conditions created optimal conditions for nighttime long-wave radiation loss (Figure 10c).

At the lower transect, the inversion development was characterized by more rapid cooling at lower vs. higher elevations beginning in the midafternoon of 3 August 2012 (~15:00 PST; south facing side of the transect; Figure 10c), resulting in a transect-wide inversion within 1–2 h (by ~16:00 PST) that peaked in magnitude at 34.0°C km^{-1} at 04:00 PST on 4 August 2012 (see similar patterns for the north facing side of the lower transect and both the south and north facing sides of the upper transect in supporting information Figures S5–S7). An inversion also developed at the basin scale (RS04-RS02, Figure 11a), although it formed later (00:00 PST on 4 August 2012) and reached its maximum gradient (5.3°C km^{-1}) at 07:00 PST on 4 August 2012 (not shown).

At 06:00 PST on 4 August 2012, when temperature inversions were near their maxima, wind directions at VANMET and CENMET (nonvalley bottom meteorological stations; Figure 1) were downslope and down valley (northeasterly; Figure 11a). Wind speeds at the valley floor at PRIMET, were weak and wind direction was below detection (<0.1 m s^{-1}).

By 14:00 PST on 4 August 2012, air was moving upslope and up valley at all meteorological stations (Figure 11b). The basin-scale inversion at 06:00 PST had disappeared, and the strongly inverted temperature profile at the lower transect became roughly isothermal (Figure 11b, bottom). At the upper transect, the inversion lasted through the afternoon, due to the presence of a shallow layer of colder air at the valley floor (Figure 11b, top).

4.3.2. A Persistent Winter Cold-Air Pool

One of the longest persistent temperature inversions measured occurred from 15 to 23 January 2013 as defined by the RS04-RS02 temperature gradient (see Figures 12 and 13 and supporting information Figures S8–S10). A cold air mass moved into the region after 7 January 2013 (Figure 12a). Between 11 and 14 January 2013, warm air had replaced the cold air aloft but had not displaced the cold lower air in the Willamette Basin, resulting in a strong low-level inversion by 17 January 2013. The strong anticyclonic flow (highly negative vorticity; Figure 12b) promoted atmospheric stability. Although nighttime cloud cover was not measured, the sky was very likely cloudless based on daytime insolation (Figure 12c). On 23 January 2013, clouds moved over the Andrews Forest, precipitation was measured that afternoon, and the basin-scale inversion broke up by 14:00 PST (not shown). The inversion persisted a few days longer at the transects than at the basin scale and about 8 h longer at the basin scale than in the ERA5 data.

A few days before the onset of the persistent inversion (08:00 PST, 11 January 2013), temperature gradients from ERA5, and at RS04, RS02, and the upper and lower transects all displayed very similar profiles with a near-standard environmental temperature gradient of −6.5°C km^{-1} (Figure 13a), implying vertical mixing of air occurring from the regional scale down to small, narrow valleys, and below the canopy.

By 15:00 PST on 19 January 2013, temperature gradients at the transects were near their maximum values (44°C km^{-1} and 85°C km^{-1} at the lower and upper transects, respectively) during this persistent inversion (Figure 13b). Wind direction at PRIMET on this afternoon was down valley (Figure 12c). Wind direction at CENMET and UPLMET was also downslope, with only VANMET showing upslope, albeit weak, winds (Figure 13b). The different wind direction at VANMET (upslope) compared to the winds at the other

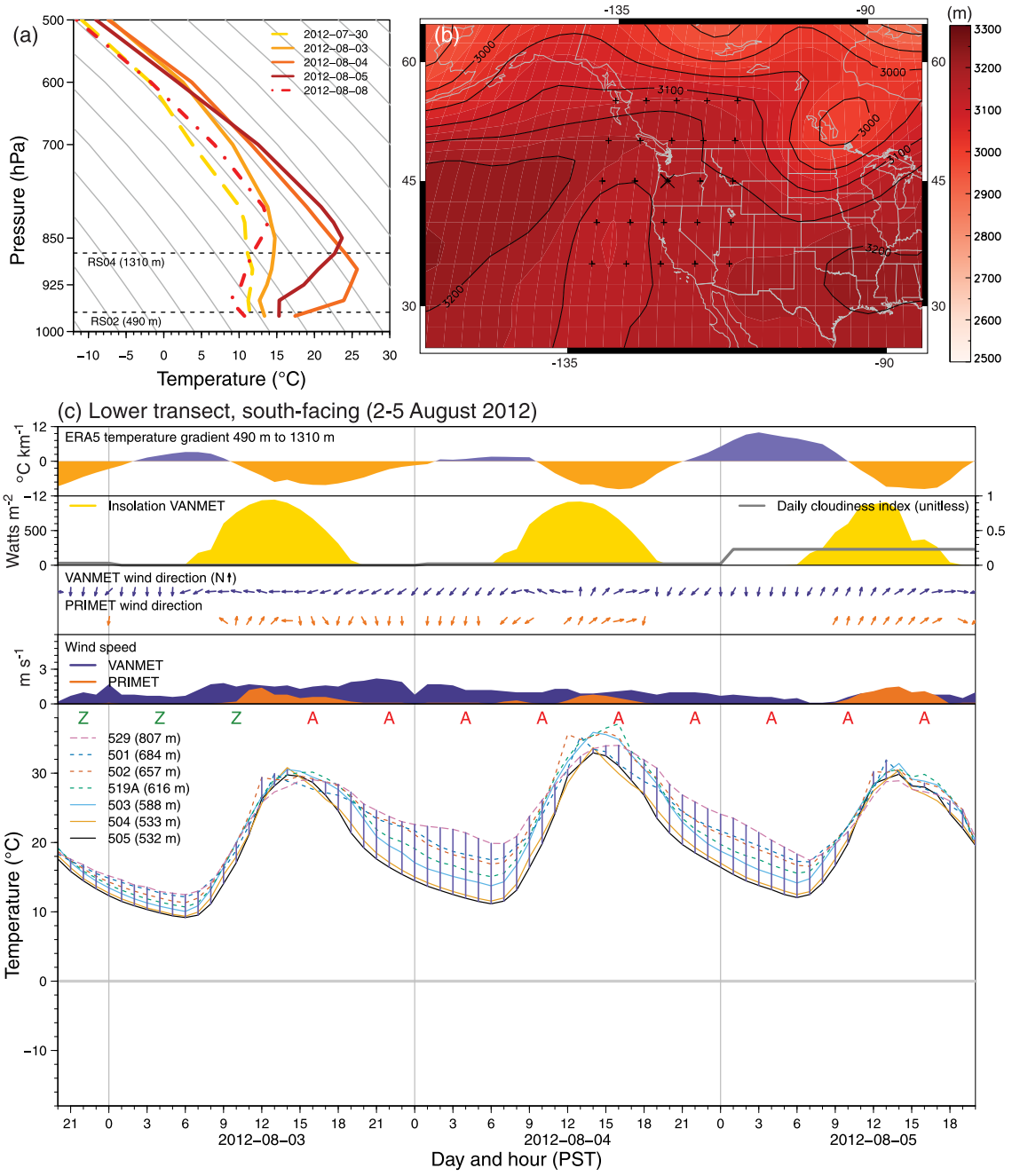

Figure 10. (a) Vertical air temperature profiles for selected nights before, during, and after strong temperature gradient inversions at Andrews Forest on 4 August 2012. Temperature and pressure are from ERA5 at 12 UTC (04:00 PST) for the grid point ~65 km west of the Andrews Forest. Horizontal dashed lines show the vertical position (in approximate pressure coordinates) of the RS02 and RS04 temperature sensors, and gray lines show profiles with a gradient of −6.5°C km^{-1}. (b) NCEP NCAR R1 700-hPa geopotential heights on 4 August 2012 at 12 UTC (04:00 PST). The "+" symbols indicate the NCEP NCAR R1 grid points used to calculate the flow curvature index centered on "×," the closest grid point to the Andrews Forest. (c) Time series of environmental variables and hourly temperature at the south facing lower transect from 2 August 2012, 20:00 PST, to 5 August 2012, 20:00 PST. Vertical purple lines (bottom plots in each panel) show the presence of inversions from the lowest sensor on the transect (sensor 505) to the highest sensor on the transect that is also warmer than sensor 505. The letters "Z" (zonal flow) and "A" (anticyclonic) give the synoptic flow classification at 6-h intervals. See supporting information Figure S4 for an expanded description of panel (c). Note that temperature data displayed in (c) are observations before adjusting for radiation-produced temperature errors (see section 2.3.3). The vertical gray lines indicate midnight. Panel (c) is a single image adapted from animations spanning November 2005 through December 2018 (Rupp et al., 2020).

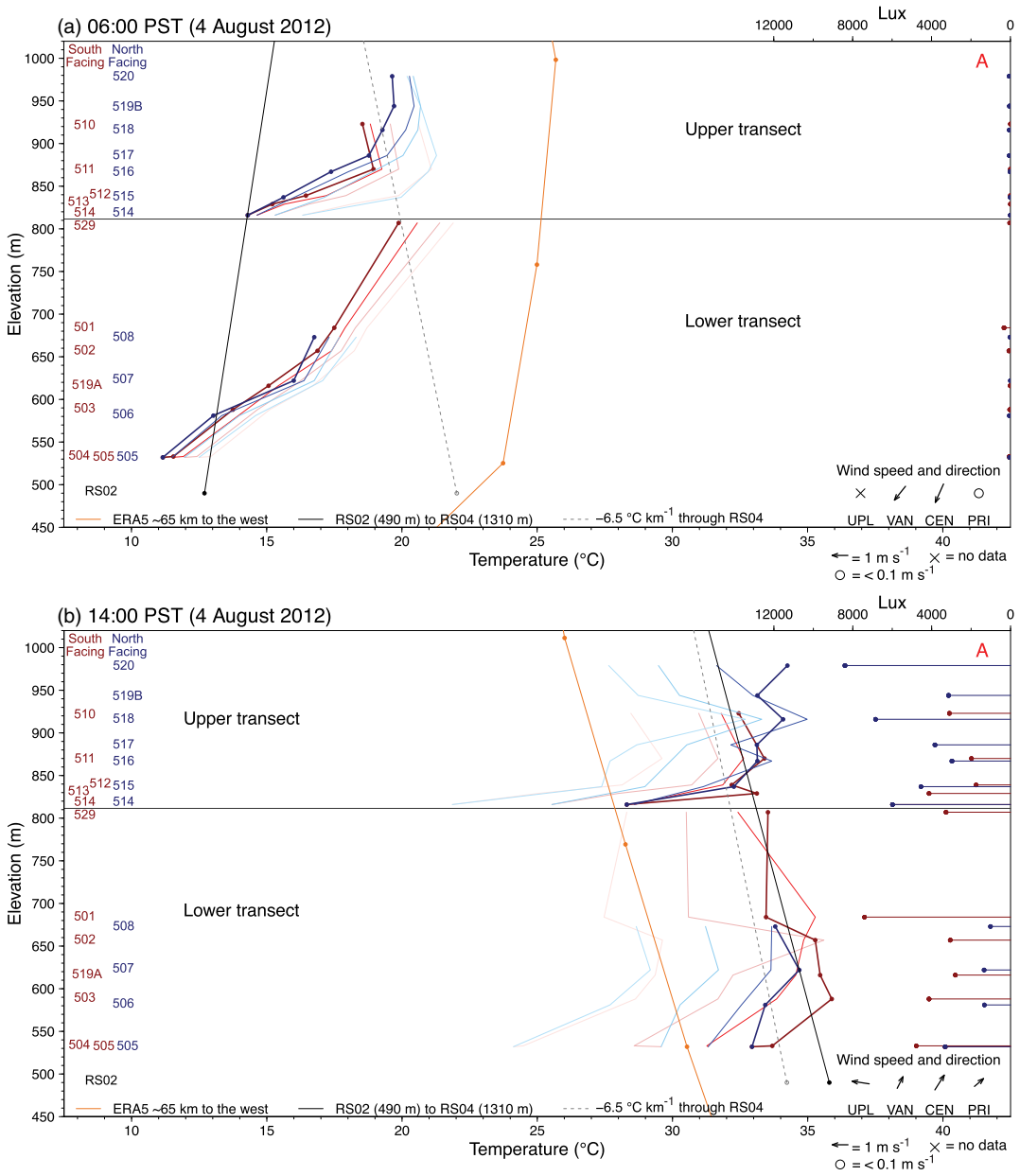

Figure 11. Elevation vs. temperature and illumination along the lower and upper transects at (a) 06:00 PST and (b) 14:00 PST on 4 August 2012. Progressively lighter blue and red lines show the temperature profiles at 1, 2, and 3 h prior. The gray horizontal line separates the lower (bottom of each panel) and upper (top of each panel) transect sensors. Transect temperature data displayed are observations before adjusting for radiation-produced temperature errors (section 2.3.3). Additional diagnostic variables displayed include wind speed and direction at CENMET (CEN), PRIMET (PRI), UPLMET (UPL), and VANMET (VAN); the RS04-RS02 temperature profile (solid black line); a hypothetical RS04-RS02 temperature profile based on the standard temperature gradient of −6.5°C km^{-1} and the temperature at RS04 (dashed gray line); and the ERA5 temperature profile between 436 and 1,310 m (orange line). Note that RS04 at 1,310 m is outside the range of the *y*-axis. Site identification numbers indicate the sensor elevations for south facing (red) and north facing (blue) sites. Panels (a) and (b) are single images adapted from animations spanning November 2005 through December 2018 (Rupp et al., 2020).

stations (downslope) suggest that, despite the clear sky, the insolation-driven afternoon upward air movement did not extend to the lower part of the basin and was therefore insufficient to break up the strongly stable and deep cold-air pool. We note also that inversions were stronger during daylight hours overall.

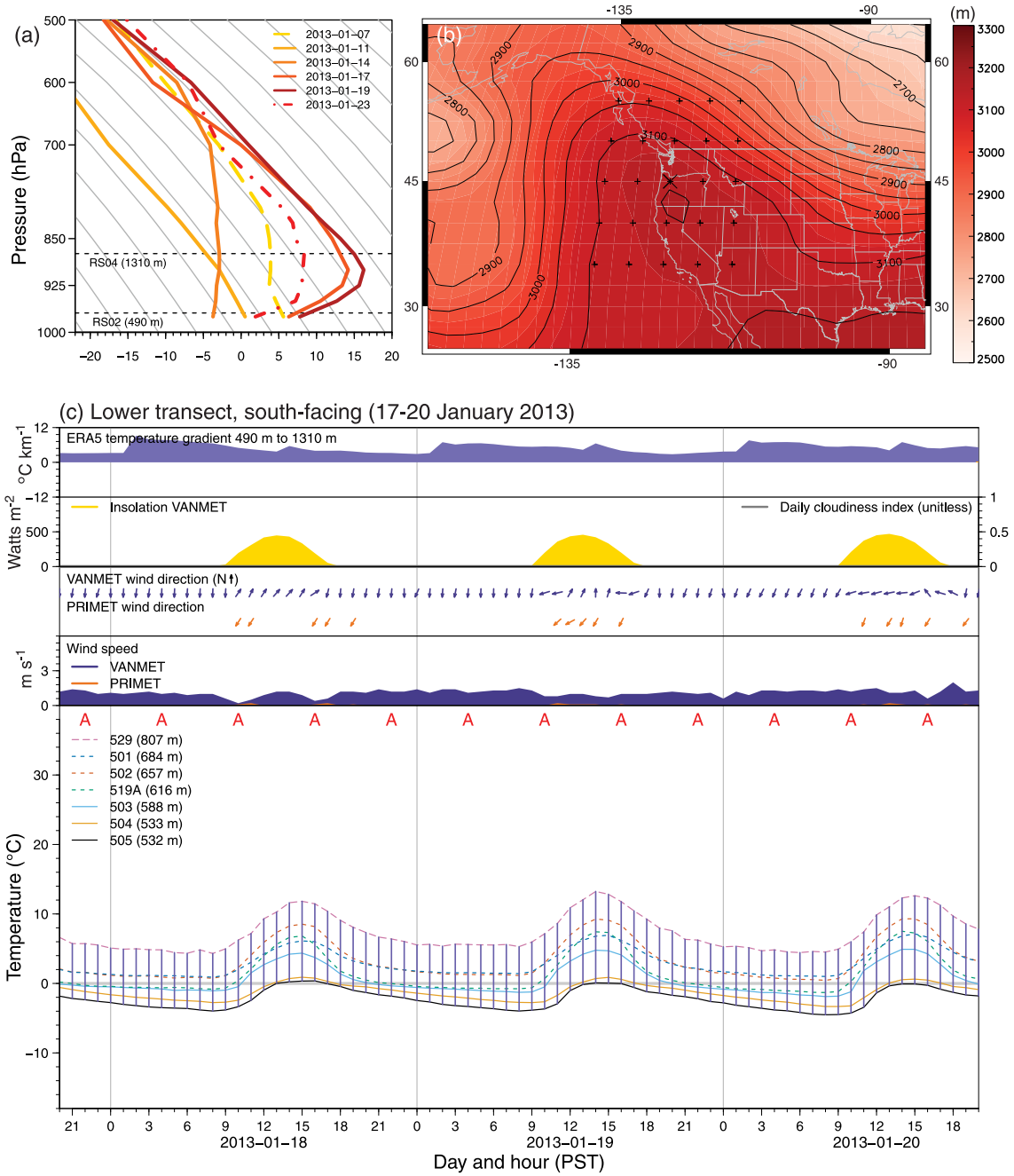

Figure 12. (a) Vertical air temperature profiles for selected nights before, during, and after strong temperature gradient inversions at Andrews Forest on 19 January 2013. (b) NCEP NCAR R1 700-hPa geopotential heights on 19 January 2013 at 12 UTC (04:00 PST). (c) Time series of environmental variables and hourly temperature at the south-facing lower transect from 17 January 2013, 20:00 PST, to 20 January 2013, 20:00 PST. See Figure 10 for additional details and supporting information Figure S4 for an expanded description of panel (c).

5. Discussion

5.1. A Climatology of Temperature Gradients and Inversions

Seasonal variations in temperature inversion frequency at the Andrews Forest result from intra-annual variations in synoptic-scale and local controls. In winter, short days and low Sun angles promote the rapid formation of both daytime and nighttime inversions when clear-sky conditions occur. The strongest, most persistent winter inversions (lasting several days) form when warm air aloft moves into the region but

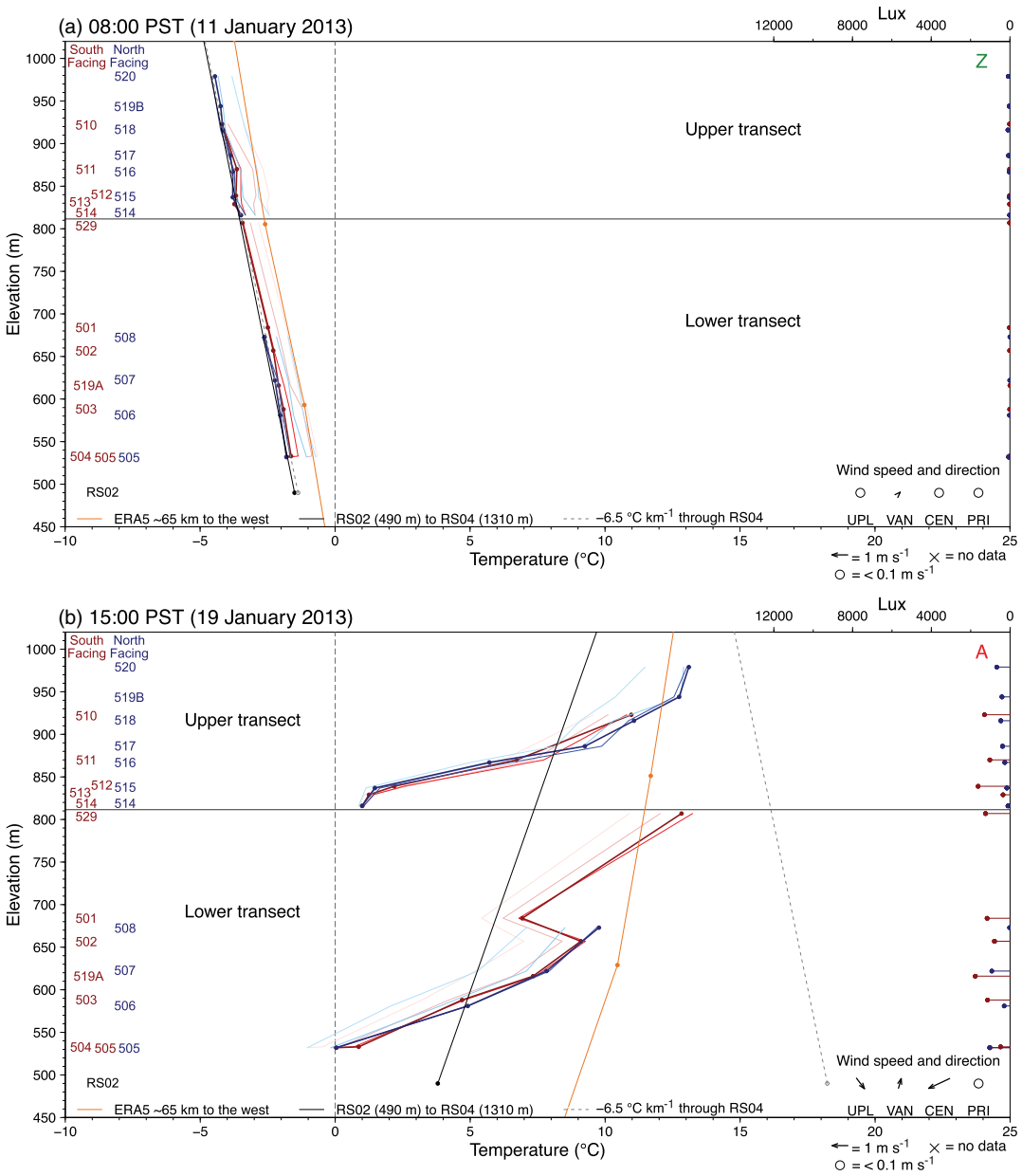

Figure 13. Same as Figure 11 but for (a) 11 January 2013 at 08:00 PST and (b) 19 January 2013 at 15:00 PST.

does not mix down into existing stable, cold-air pools. The deeply incised valleys of the Andrews Forest limit the effectiveness of vertical mixing in these valleys, reinforcing inversion formation and persistence.

In spring, increased solar radiation loading warms the surface at a generally faster rate than the free atmosphere, resulting in relatively steep, negative temperature gradients regionwide, during both day and night. Cloudiness decreases compared to winter values (Figure 3a), promoting vertical mixing during the day and decreases in inversion frequency at all spatial scales. The persistent snow cover at higher elevations in early spring may also reduce basin-scale temperature gradients by keeping the higher-elevation surfaces cooler by means of snow's reflective, radiative, and latent heat properties.

In summer, a major synoptic transition occurs between June and July; early July typically marks the beginning of a reliably dry, calm summer period, with few clouds and high solar radiation loading. Nighttime inversion frequency increases markedly during this transition period, as optimal conditions for cold-air

drainage and pooling become typical. Strong solar heating during the day effectively breaks up inversions at the synoptic and basin scales, but the transects, sheltered by topography and both sheltered and shaded by forest canopy, experience an increase in daytime inversion frequency, indicating that air drainage and pooling are occurring in protected valleys and depressions throughout the Andrews Forest in summer.

The dry, calm weather typical of summer often persists into September, when clear-sky insolation values are similar to those in spring. Days become shorter, but inversion conditions are still near optimal, and nighttime inversion frequency remains high, reaching a maximum at the basin scale. The transition back to cloudy conditions characteristic of winter normally occurs in October, with an associated decrease in inversion frequency at all spatial scales. Inversion frequency then increases again in winter, as solar heating wanes.

5.2. Synoptic- and Local-Scale Controls Affecting Temperature Gradients

5.2.1. Synoptic- to Local-Scale Weather

In the absence of surface and boundary-layer influences, temperature gradients based on near-surface temperature measurements at different elevations within the Andrews Forest would track variations in the vertical free-air temperature gradient over the Willamette Valley, and the high explanatory power of the ERA5 temperature gradient in the multivariate linear regression models (Figures 9a and 9b) implies a strong influence of free-air temperature on near-surface temperature. The strength of this influence, however, is reduced in progressively smaller and narrower valleys that are more sheltered from insolation and the regional air flow.

Although near-surface temperature often covaries with upper-air temperature, the relatively high explanatory power of the vorticity index (Figure 9) suggests that synoptic anticyclonic (A) regional air flow patterns promote decoupling of near-surface and upper air, whereas cyclonic (C) patterns promote vertical mixing of air (Daly et al., 2010). We were surprised that the flow strength index showed such little importance given that Daly et al. (2010) found it a sizable influence on VANMET-PRIMET gradients in daily minimum temperature. Because cloudiness and flow strength are correlated ($r = 0.54$), the effect of flow strength may partly be represented by cloudiness in regression model results.

When insolation is not a confounding factor, the influence of synoptic-scale circulation and local cloud cover is similar whether the temperature measurements are made in an open clearing or under the forest canopy, or at the basin scale versus in a narrow valley (Figures 9a and 9c). Moreover, while the nighttime inversion frequencies are very different between the basin and transect scales, the intra-annual variations in inversion frequency are very similar (Figure 3c). This coherency in inversion patterns across all our basin-scale and cross-valley-scale measurements implies that seasonally varying synoptic-scale circulation patterns regulate nighttime inversions similarly despite spatial variations in topography and forest cover.

Although synoptic and local weather variability is helpful for understanding the causes of seasonal patterns in temperature gradients, a large amount of the variability in temperature gradients remains unexplained. A close inspection of the data, particularly via the animations accompanying this study's data set (Rupp et al., 2020), reveals complexities that will require additional analyses to understand, and frequent temperature gradient inversion episodes that do not conform to the canonical conditions under which cold-air pools are expected to exist (e.g., inversions persisting at the transects for more than 48 h under overcast conditions, continual rain, upslope winds above the canopy, and no basin-scale inversion even at night).

5.2.2. Insolation, Topography, and the Forest Canopy

Daily clear-sky insolation, which changes gradually during the year as Sun angle and day length vary, provides the potential for surface heating and upslope wind development. Although surface heating effects may be dampened under canopy, strong upslope wind above the canopy can drive upslope wind below it (e.g., Belcher et al., 2012). The high frequency and long duration of persistent midwinter inversions is likely a result of protracted shading produced by low Sun angles in this mountain landscape, as found in studies conducted elsewhere (e.g., Reeves & Stensrud, 2009; Whiteman et al., 2001). The generally high explanatory power of daily clear-sky insolation (estimated for an unobstructed, horizontal surface) in multivariate linear regression models of afternoon temperature gradients (Figure 9) suggests that seasonal variation in shading is an important factor governing midday conditions.

In addition to providing shade, topographic features may also direct flows of cold-air drainage and pooling (Daly et al., 2010). For example, cold-air pools may form more frequently at PRIMET, which is located on a valley floor, than at RS02, which is located on a 22° slope and at a higher elevation than PRIMET. These topographic differences may help to explain why VANMET-PRIMET has higher nighttime inversion frequencies than RS04-RS02 from November to May (Figures 2 and 3).

Forest canopy cover, which varies across the Andrews Forest as a result of past disturbances (e.g., landslides), land use activities (e.g., logging), and site effects on tree growth (e.g., slope aspect and soil properties), may interact with insolation and topography to affect the development of cold-air drainage (e.g., Kiefer & Zhong, 2013, 2015; Whiteman, 1986, 1990). During the day, insolation heats the canopy foliage and can create a strong inversion between the ground and the canopy base, allowing for drainage flow to persist all day under the canopy even while above the canopy, the inversion breaks up and the air flows upslope. This decoupling of below- and above-canopy flow was observed by Pypker et al. (2007a) in a small, V-shaped valley in the western end of the Andrews Forest (Watershed 1). Although we do not have the wind measurements to confirm it, the relatively high frequency of summer daytime inversions at the transects, particularly at the upper transect, is consistent with this decoupling process. During persistent winter inversions, transect inversions can be stronger during the day than at night (e.g., Figure 12c). These stronger daytime inversions could also be caused by stronger subcanopy inversions as the Sun warms the foliage. However, they could also be the result of valley bottoms simply being more topographically shaded and sheltered from ventilation in winter. Our study did not attempt to separate the effects of topography and forest canopy.

Shading provided by the forest canopy also affects snowpack persistence, which in turn affects heat transfer, local air temperature, and resulting temperature gradients (e.g., Dorninger et al., 2011; Zängl, 2005). Snowpack persists longer at upper elevations and under forest canopy in this landscape (Marks et al., 1998). Although snow data are not available for RS04, it is likely that the combination of topographic and canopy shading allows the RS04 site to maintain a substantial snowpack for longer duration than the open VANMET site, which may partly explain the lower frequency of inversions detected at the high- and low-elevation forested sites (RS04-RS02) compared to the high- and low-elevation sites without canopy cover (VANMET-PRIMET).

Variations in forest canopy cover combined with steep terrain and seasonal changes in Sun angle may lead to illumination of sensor sites by sunflecks (e.g., supporting information Figure S1e) or more direct illumination (e.g., supporting information Figure S1f) for short periods of time. These illumination events may produce ephemeral temperature increases at individual naturally aspirated sensor sites (e.g., see sensor 520 in Figure 11b), which, if the sites are at high elevations, may result in measured temperature inversions that are not the result of cold-air drainage. At the transects, we attempted to remove the effect of direct solar heating of the sensors by excluding times with very high illumination values and by using an illumination-based adjustment to temperature.

5.3. Cold-Air Pooling Under Climate Change

Better understanding of when, where, and how cold-air pools form may be relevant to ongoing discussions about the effects of climate change in mountain landscapes. Although cold-air pools may be warmer under projected future climate changes, they may still be able to mitigate some potential future climate change effects by maintaining suitable microclimatic conditions for species and ecosystems (Dobrowski et al., 2009; Morelli et al., 2016). The assumption that cold-air pools break up during the day and thus may not affect maximum daytime temperature as climate changes (Curtis et al., 2014) is not supported by our results, which found relatively frequent summer daytime temperature inversions at the cross-valley scale.

Potential future climate change may also alter the larger-scale atmospheric conditions that promote near-surface temperature inversions (Ji et al., 2019). If climate change produces synoptic-scale conditions that increase cold-air pooling occurrence (e.g., more anticyclonic conditions), valleys may be more frequently decoupled from the upper atmosphere in the future and hence "buffered" from some of the effects of climate warming, whereas if climate change produces synoptic conditions that reduce cold-air pooling occurrence (e.g., more cyclonic conditions), valleys may be less frequently decoupled from the upper atmosphere and less buffered from some of the effects of climate warming (Daly et al., 2010; Pepin & Lundquist, 2008; Pepin et al., 2011). Projections from climate models forced with increasing greenhouse

gas concentrations indicate a pattern of more anticyclonic conditions in summer and more cyclonic conditions in winter over the northwestern United States, but the uncertainty in these changes is large (Rupp, Abatzoglou, et al., 2017; Rupp, Li, et al., 2017). In addition, the association of fine-scale temperature inversions with topographic features implies that cold-air drainage and pooling may persist in forested mountain landscapes, despite future alterations in synoptic conditions. These findings are relevant to understanding how climate changes projected by climate models (i.e., general circulation models) may be expressed at local scales and indicate the importance of including the interactions of synoptic atmospheric conditions with local topography and insolation in both dynamic and statistical downscaling of climate model simulations (e.g., Burns & Chemel, 2014; Curtis et al., 2014).

6. Conclusion

Analysis of 13 years of hourly air temperature data indicates temperature inversion frequency in this steep forested mountain landscape results from the interplay of synoptic-scale and local controls. Cold-air pools identified from near-surface air temperature inversions are more likely to occur at finer spatial scales: Inversion frequency and persistence were much lower based on basin-scale near-surface measurements (~10-km horizontal and ~0.8-km vertical extents) than from finer-scale (~1-km horizontal and ~0.2-km vertical) measurements along cross-valley transects. Inversions were frequent in winter and often persisted for several days even at the basin scale, while in summer inversions persisting through the daytime were only detected at the finest cross-valley scale. Nighttime inversions were most frequent in winter and in summer compared to spring and early fall. The intra-annual pattern of nighttime inversions was similar at the basin- and cross-valley scales of measurement. This intra-annual pattern was also similar for basin-scale temperature gradients based on sensors in open clearings or beneath dense canopy. This coherency in the intra-annual nighttime inversion patterns across all our sites implies that seasonally varying synoptic-scale circulation patterns regulate these nocturnal events similarly despite spatial variations in topography and forest cover.

In contrast, the intra-annual pattern of daytime inversions differed between the basin and cross-valley scales and between two topographically distinct cross-valley transects, implying that topographic effects on insolation and local winds were key controls. The high frequency of inversions (>50% of hours) measured at the transect scale implies that cold-air pooling is the norm, and not the exception, within the Andrews Forest and likely other similar landscapes in the western Cascade Range.

Data Availability Statement

Data were provided by the H.J. Andrews Experimental Forest and Long Term Ecological Research program, administered cooperatively by the USDA Forest Service Pacific Northwest Research Station, Oregon State University, and the Willamette National Forest, and supported by the National Science Foundation (Andrews Forest LTER7 DEB-1440409). ERA5 data are available on the Copernicus Climate Change Service Climate Data Store (https://cds.climate.copernicus.eu). NCEP Reanalysis data are available from the NOAA/OAR/ESRL Physical Sciences Division (Boulder, Colorado, USA; https://www.esrl.noaa.gov/psd/data/gridded/data.ncep.reanalysis.html). Additional data used in this study are available from Daly and McKee (2016, 2019), Daly (2017), and Rupp et al. (2020).

Acknowledgments

We thank Eric Kelsey for comments on an earlier version of the manuscript and Michael Halbleib for creating the maps in Figure 1. D. R. was supported by the U.S. Geological Survey (USGS; cooperative agreement G12AC20283). S. S. was supported by the USGS Climate Research & Development Program. J. J. and D. R. were supported by the National Science Foundation (Andrews Forest LTER7 DEB-1440409). C. D. and D. R. were supported by the USDA Risk Management Agency (cooperative agreement 2019-2363). Any use of trade, firm, or product names is for descriptive purposes only and does not imply endorsement by the U.S. Government.

References

Arduini, G., Chemel, C., & Staquet, C. (2020). Local and non-local controls on a persistent cold-air pool in the Arve River Valley. *Quarterly Journal of the Royal Meteorological Society*. https://doi.org/10.1002/qj.3776

Barr, S., & Orgill, M. M. (1989). Influence of external meteorology on nocturnal valley drainage winds. *Journal of Applied Meteorology*, *28*(6), 497–517. https://doi.org/10.1175/1520-0450(1989)028<0497:IOEMON>2.0.CO;2

Belcher, S. E., Harman, I. N., & Finnigan, J. J. (2012). The wind in the willows: Flows in forest canopies in complex terrain. *Annual Review of Fluid Mechanics*, *44*(1), 479–504. https://doi.org/10.1146/annurev-fluid-120710-101036

Burns, P., & Chemel, C. (2014). Evolution of cold-air-pooling processes in complex terrain. *Boundary-Layer Meteorology*, *150*(3), 423–447. https://doi.org/10.1007/s10546-013-9885-z

Corripio, J. G. (2019). *insol: solar radiation, R package version 1.2 [Computer software]*. Retrieved from https://CRAN.R-project.org/package=insol

Cramer, O. P., & Lynott, R. E. (1961). Cross-section analysis in the study of windflow over mountainous terrain. *Bulletin of the American Meteorological Society*, *42*(10), 693–702. https://doi.org/10.1175/1520-0477-42.10.693

Curtis, J. A., Flint, L. E., Flint, A. L., Lundquist, J. D., Hudgens, B., Boydston, E. E., & Young, J. K. (2014). Incorporating cold-air pooling into downscaled climate models increases potential refugia for snow-dependent species within the Sierra Nevada Ecoregion, CA. *PLoS ONE*, *9*(9), e106984. https://doi.org/10.1371/journal.pone.0106984

Daly, C. (2017). *Cold air drainage transect studies at the Andrews Experimental Forest, 2002 to present*. Corvallis, OR: Long-Term Ecological Research. Forest Science Data Bank. https://doi.org/10.6073/pasta/a701c8b93c527690b823e50a3efa10b5

Daly, C., Conklin, D. R., & Unsworth, M. H. (2010). Local atmospheric decoupling in complex topography alters climate change impacts. *International Journal of Climatology*, *30*(12), 1857–1864. https://doi.org/10.1002/joc.2007

Daly, C., & McKee, W. (2016). *Air and soil temperature data from the Reference Stand network at the Andrews Experimental Forest, 1971 to present*. Corvallis, OR: Long-Term Ecological Research. Forest Science Data Bank. https://doi.org/10.6073/pasta/75d4bff8a8824977126c25f7763d8ae3

Daly, C., & McKee, W. (2019). *Meteorological data from benchmark stations at the Andrews Experimental Forest, 1957 to present*. Corvallis, OR: Long-Term Ecological Research. Forest Science Data Bank. https://doi.org/10.6073/pasta/c96875918bb9c86d330a457bf4295cd9

De Wekker, S. F. J., & Whiteman, C. D. (2006). On the time scale of nocturnal boundary layer cooling in valleys and basins and over plains. *Journal of Applied Meteorology and Climatology*, *45*(6), 813–820. https://doi.org/10.1175/JAM2378.1

Dobrowski, S. Z. (2011). A climatic basis for microrefugia: The influence of terrain on climate. *Global Change Biology*, *17*(2), 1022–1035. https://doi.org/10.1111/j.1365-2486.2010.02263.x

Dobrowski, S. Z., Abatzoglou, J. T., Greenberg, J. A., & Schladow, S. G. (2009). How much influence does landscape-scale physiography have on air temperature in a mountain environment? *Agricultural and Forest Meteorology*, *149*(10), 1751–1758. https://doi.org/10.1016/j.agrformet.2009.06.006

Dorai-Raj, S. (2014). *binom: Binomial confidence intervals for several parameterizations, R package version 1.1-1 [Computer software]*. Retrieved from https://CRAN.R-project.org/package=binom

Dorninger, M., Whiteman, C. D., Bica, B., Eisenbach, S., Pospichal, B., & Steinacker, R. (2011). Meteorological events affecting cold-air pools in a small basin. *Journal of Applied Meteorology and Climatology*, *50*(11), 2223–2234. https://doi.org/10.1175/2011JAMC2681.1

Dye, A. W., Rastogi, B., Clemesha, R. E. S., Kim, J. B., Samelson, R. M., Still, C. J., & Williams, A. P. (2020). Spatial patterns and trends of summertime low cloudiness for the Pacific Northwest, 1996–2017. *Geophysical Research Letters*, *47*, e2020GL088121. https://doi.org/10.1029/2020GL088121

Elith, J., Leathwick, J. R., & Hastie, T. (2008). A working guide to boosted regression trees. *Journal of Animal Ecology*, *77*(4), 802–813. https://doi.org/10.1111/j.1365-2656.2008.01390.x

Fridley, J. D. (2009). Downscaling climate over complex terrain: High finescale (<1000 m) spatial variation of near-ground temperatures in a montane forested landscape (Great Smoky Mountains). *Journal of Applied Meteorology and Climatology*, *48*(5), 1033–1049. https://doi.org/10.1175/2008JAMC2084.1

Froelich, N. J., & Schmid, H. P. (2006). Flow divergence and density flows above and below a deciduous forest: Part II. Below-canopy thermotopographic flows. *Agricultural and Forest Meteorology*, *138*(1–4), 29–43. https://doi.org/10.1016/j.agrformet.2006.03.013

Grömping, U. (2006). Relative importance for linear regression in R: The package relaimpo. *Journal of Statistical Software*, *17*(1). Retrieved from https://doi.org/10.18637/jss.v017.i01

Gustavsson, T., Karlsson, M., Bogren, J., & Lindqvist, S. (1998). Development of temperature patterns during clear nights. *Journal of Applied Meteorology*, *37*(6), 559–571. https://doi.org/10.1175/1520-0450(1998)037<0559:DOTPDC>2.0.CO;2

Hersbach, H., Bell, B., Berrisford, P., Hirahara, S., Horányi, A., Muñoz-Sabater, J., et al. (2020). The ERA5 global reanalysis. *Quarterly Journal of the Royal Meteorological Society*, *146*(730), 1999–2049. https://doi.org/10.1002/qj.3803

Hijmans, R. J., Phillips, S., Leathwick, J., & Elith, J. (2017). *dismo: Species distribution modeling, R package version 1.1-4 [Computer software]*. Retrieved from https://CRAN.R-project.org/package=dismo

Jemmett-Smith, B., Ross, A. N., & Sheridan, P. (2018). A short climatological study of cold air pools and drainage flows in small valleys. *Weather*, *73*(8), 256–262. https://doi.org/10.1002/wea.3281

Jenkinson, A., & Collison, F. (1977). An initial climatology of gales over the North Sea. In *Synoptic Climatology Branch Memorandum No. 62* (pp. 1–62). Bracknell, UK: Meteorol. Off.

Ji, F., Evans, J. P., Di Luca, A., Jiang, N., Olson, R., Fita, L., et al. (2019). Projected change in characteristics of near surface temperature inversions for southeast Australia. *Climate Dynamics*, *52*(3–4), 1487–1503. https://doi.org/10.1007/s00382-018-4214-3

Johnson, J. W., & LeBreton, J. M. (2004). History and use of relative importance indices in organizational research. *Organizational Research Methods*, *7*(3), 238–257. https://doi.org/10.1177/1094428104266510

Joly, D., & Richard, Y. (2019). Frequency, intensity, and duration of thermal inversions in the Jura Mountains of France. *Theoretical and Applied Climatology*, *138*(1–2), 639–655. https://doi.org/10.1007/s00704-019-02855-3

Kalnay, E., Kanamitsu, M., Kistler, R., Collins, W., Deaven, D., Gandin, L., et al. (1996). The NCEP/NCAR 40-year reanalysis project. *Bulletin of the American Meteorological Society*, *77*(3), 437–471. https://doi.org/10.1175/1520-0477(1996)077<0437:TNYRP>2.0.CO;2

Kelsey, E. P., Cann, M. D., Lupo, K. M., & Haddad, L. J. (2019). Synoptic to microscale processes affecting the evolution of a cold-air pool in a northern New England forested mountain valley. *Journal of Applied Meteorology and Climatology*, *58*(6), 1309–1324. https://doi.org/10.1175/JAMC-D-17-0329.1

Kiefer, M. T., & Zhong, S. (2013). The effect of sidewall forest canopies on the formation of cold-air pools: A numerical study. *Journal of Geophysical Research: Atmospheres*, *118*, 5965–5978. https://doi.org/10.1002/jgrd.50509

Kiefer, M. T., & Zhong, S. (2015). The role of forest cover and valley geometry in cold-air pool evolution. *Journal of Geophysical Research: Atmospheres*, *120*, 8693–8711. https://doi.org/10.1002/2014JD022998

Lareau, N. P., Crosman, E., Whiteman, C. D., Horel, J. D., Hoch, S. W., Brown, W. O. J., & Horst, T. W. (2013). The persistent cold-air pool study. *Bulletin of the American Meteorological Society*, *94*(1), 51–63. https://doi.org/10.1175/BAMS-D-11-00255.1

Lenoir, J., Hattab, T., & Pierre, G. (2017). Climatic microrefugia under anthropogenic climate change: Implications for species redistribution. *Ecography*, *40*(2), 253–266. https://doi.org/10.1111/ecog.02788

Losleben, M., Pepin, N., & Pedrick, S. (2000). Relationships of precipitation chemistry, atmospheric circulation, and elevation at two sites on the Colorado front range. *Atmospheric Environment*, *34*(11), 1723–1737. https://doi.org/10.1016/S1352-2310(99)00431-8

Mahrt, L., Lee, X., Black, A., Neumann, H., & Staebler, R. M. (2000). Nocturnal mixing in a forest subcanopy. *Agricultural and Forest Meteorology*, *101*(1), 67–78. https://doi.org/10.1016/S0168-1923(99)00161-6

Malek, A. (2019). *Empirical analysis of processes affecting drainage flows and inversions in a forested mountain landscape* (PhD dissertation). Corvallis, U.S.A: Oregon State University.

Marks, D., Kimball, J., Tingey, D., & Link, T. (1998). The sensitivity of snowmelt processes to climate conditions and forest cover during rain-on-snow: A case study of the 1996 Pacific Northwest flood. *Hydrological Processes*, *12*(10–11), 1569–1587. https://doi.org/10.1002/(SICI)1099-1085(199808/09)12:10/11<1569::AID-HYP682>3.0.CO;2-L

Marvin, C. F. (1914). Air drainage explained. *Monthly Weather Review*, *42*(10), 583–585. https://doi.org/10.1175/1520-0493(1914)42<583:ADE>2.0.CO;2

Mass, C. F., Albright, M. D., & Brees, D. J. (1986). The onshore surge of marine air into the Pacific Northwest: A coastal region of complex terrain. *Monthly Weather Review*, *114*(12), 2602–2627. https://doi.org/10.1175/1520-0493(1986)114<2602:TOSOMA>2.0.CO;2

Miró, J. R., Peña, J. C., Pepin, N., Sairouni, A., & Aran, M. (2018). Key features of cold-air pool episodes in the northeast of the Iberian Peninsula (Cerdanya, eastern Pyrenees). *International Journal of Climatology*, *38*(3), 1105–1115. https://doi.org/10.1002/joc.5236

Mock, C. J. (1996). Climatic controls and spatial variations of precipitation in the western United States. *Journal of Climate*, *9*(5), 1111–1125. https://doi.org/10.1175/1520-0442(1996)009<1111:CCASVO>2.0.CO;2

Morelli, T. L., Daly, C., Dobrowski, S. Z., Dulen, D. M., Ebersole, J. L., Jackson, S. T., et al. (2016). Managing climate change refugia for climate adaptation. *PLoS ONE*, *11*(8), e0159909. https://doi.org/10.1371/journal.pone.0159909

Nakamura, R., & Mahrt, L. (2005). Air temperature measurement errors in naturally ventilated radiation shields. *Journal of Atmospheric and Oceanic Technology*, *22*(7), 1046–1058. https://doi.org/10.1175/JTECH1762.1

NOAA (1976). *U.S. standard atmosphere, 1976* (No. NOAA-S/T 76-1562). Washington, D.C.: National Oceanic and Atmospheric Administration.

Novick, K. A., Oishi, A. C., & Miniat, C. F. (2016). Cold air drainage flows subsidize montane valley ecosystem productivity. *Global Change Biology*, *22*(12), 4014–4027. https://doi.org/10.1111/gcb.13320

Pagès, M., Pepin, N., & Miró, J. R. (2017). Measurement and modelling of temperature cold pools in the Cerdanya valley (Pyrenees), Spain. *Meteorological Applications*, *24*(2), 290–302. https://doi.org/10.1002/met.1630

Pepin, N. C., Daly, C., & Lundquist, J. (2011). The influence of surface versus free-air decoupling on temperature trend patterns in the western United States. *Journal of Geophysical Research*, *116*, D10109. https://doi.org/10.1029/2010JD014769

Pepin, N. C., & Lundquist, J. D. (2008). Temperature trends at high elevations: Patterns across the globe. *Geophysical Research Letters*, *35*, L14701. https://doi.org/10.1029/2008GL034026

Pike, G., Pepin, N. C., & Schaefer, M. (2013). High latitude local scale temperature complexity: The example of Kevo Valley, Finnish Lapland. *International Journal of Climatology*, *33*(8), 2050–2067. https://doi.org/10.1002/joc.3573

Price, J. D., Vosper, S., Brown, A., Ross, A., Clark, P., Davies, F., et al. (2011). COLPEX: Field and numerical studies over a region of small hills. *Bulletin of the American Meteorological Society*, *92*(12), 1636–1650. https://doi.org/10.1175/2011BAMS3032.1

Pypker, T. G., Unsworth, M. H., Lamb, B., Allwine, E., Edburg, S., Sulzman, E., et al. (2007). Cold air drainage in a forested valley: Investigating the feasibility of monitoring ecosystem metabolism. *Agricultural and Forest Meteorology*, *145*(3-4), 149–166. https://doi.org/10.1016/j.agrformet.2007.04.016

Pypker, T. G., Unsworth, M. H., Mix, A. C., Rugh, W., Ocheltree, T., Alstad, K., & Bond, B. J. (2007). Using nocturnal cold air drainage flow to monitor ecosystem processes in complex terrain. *Ecological Applications*, *17*(3), 702–714. https://doi.org/10.1890/05-1906

Reeves, H. D., & Stensrud, D. J. (2009). Synoptic-scale flow and valley cold pool evolution in the western United States. *Weather and Forecasting*, *24*(6), 1625–1643. https://doi.org/10.1175/2009WAF2222234.1

Rupp, D. E., Abatzoglou, J. T., & Mote, P. W. (2017). Projections of 21st century climate of the Columbia River basin. *Climate Dynamics*, *49*(5–6), 1783–1799. https://doi.org/10.1007/s00382-016-3418-7

Rupp, D. E., Li, S., Mote, P. W., Shell, K. M., Massey, N., Sparrow, S. N., et al. (2017). Seasonal spatial patterns of projected anthropogenic warming in complex terrain: A modeling study of the western US. *Climate Dynamics*, *48*(7–8), 2191–2213. https://doi.org/10.1007/s00382-016-3200-x

Rupp, D. E., Shafer, S. L., Daly, C., Jones, J. A., & Frey, S. J. K. (2020). Temperature gradients and inversions in a forested Cascade Range basin: Data release. *Zenodo*. https://doi.org/10.5281/zenodo.4266589

Staebler, R. M., & Fitzjarrald, D. R. (2005). Measuring canopy structure and the kinematics of subcanopy flows in two forests. *Journal of Applied Meteorology*, *44*(8), 1161–1179. https://doi.org/10.1175/JAM2265.1

Stevens, E. (2010). An investigation of the relationship between surface temperatures and the establishment of snowpack during October in Fairbanks, Alaska. *Atmospheric Research*, *95*(2–3), 307–313. https://doi.org/10.1016/j.atmosres.2009.04.009

Tóta, J., Fitzjarrald, D. R., & da Silva Dias, M. A. F. (2012). Amazon rainforest exchange of carbon and subcanopy air flow: Manaus LBA site—A complex terrain condition. *The Scientific World Journal*, *2012*, 1–19. https://doi.org/10.1100/2012/165067

Vitasse, Y., Klein, G., Kirchner, J. W., & Rebetez, M. (2017). Intensity, frequency and spatial configuration of winter temperature inversions in the closed La Brevine valley, Switzerland. *Theoretical and Applied Climatology*, *130*(3–4), 1073–1083. https://doi.org/10.1007/s00704-016-1944-1

Vosper, S. B., & Brown, A. R. (2008). Numerical simulations of sheltering in valleys: The formation of nighttime cold-air pools. *Boundary-Layer Meteorology*, *127*(3), 429–448. https://doi.org/10.1007/s10546-008-9272-3

Vosper, S. B., Hughes, J. K., Lock, A. P., Sheridan, P. F., Ross, A. N., Jemmett-Smith, B., & Brown, A. R. (2014). Cold-pool formation in a narrow valley. *Quarterly Journal of the Royal Meteorological Society*, *140*(679), 699–714. https://doi.org/10.1002/qj.2160

Ward, S. E., Schulze, M., & Roy, B. (2018). A long-term perspective on microclimate and spring plant phenology in the Western Cascades. *Ecosphere*, *9*(10), e02451. https://doi.org/10.1002/ecs2.2451

Watanabe, T. (1994). Bulk parameterization for a vegetated surface and its application to a simulation of nocturnal drainage flow. *Boundary-Layer Meteorology*, *70*(1–2), 13–35. https://doi.org/10.1007/BF00712521

Whiteman, C. D. (1982). Breakup of temperature inversions in deep mountain valleys: Part I. Observations. *Journal of Applied Meteorology*, *21*(3), 270–289. https://doi.org/10.1175/1520-0450(1982)021<0270:BOTIID>2.0.CO;2

Whiteman, C. D. (1986). Temperature inversion buildup in Colorado's Eagle Valley. *Meteorology and Atmospheric Physics*, *35*(4), 220–226. https://doi.org/10.1007/BF01041814

Whiteman, C. D. (1990). Observations of thermally developed wind systems in mountainous terrain. In R. M. Banta, G. Berri, W. Blumen, D. J. Carruthers, G. A. Dalu, D. R. Durran, et al. (Eds.), *Atmospheric processes over complex terrain* (pp. 5–42). Boston, MA: American Meteorological Society. https://doi.org/10.1007/978-1-935704-25-6_2

Whiteman, C. D., Bian, X., & Zhong, S. (1999). Wintertime evolution of the temperature inversion in the Colorado Plateau Basin. *Journal of Applied Meteorology*, *38*(8), 1103–1117. https://doi.org/10.1175/1520-0450(1999)038<1103:WEOTTI>2.0.CO;2

Whiteman, C. D., Pospichal, B., Eisenbach, S., Weihs, P., Clements, C. B., Steinacker, R., et al. (2004). Inversion breakup in small Rocky Mountain and Alpine basins. *Journal of Applied Meteorology*, *43*(8), 1069–1082. https://doi.org/10.1175/1520-0450(2004)043<1069:IBISRM>2.0.CO;2

Whiteman, C. D., Zhong, S., Shaw, W. J., Hubbe, J. M., Bian, X., & Mittelstadt, J. (2001). Cold pools in the Columbia Basin. *Weather and Forecasting*, *16*(4), 432–447. https://doi.org/10.1175/1520-0434(2001)016<0432:CPITCB>2.0.CO;2

Wolyn, P. G., & McKee, T. B. (1989). Deep stable layers in the intermountain western United States. *Monthly Weather Review*, *117*(3), 461–472. https://doi.org/10.1175/1520-0493(1989)117<0461:DSLITI>2.0.CO;2

Zängl, G. (2005). Dynamical aspects of wintertime cold-air pools in an alpine valley system. *Monthly Weather Review*, *133*(9), 2721–2740. https://doi.org/10.1175/MWR2996.1

Zardi, D., & Whiteman, C. D. (2013). Diurnal mountain wind systems. In F. K. Chow, S. F. J. De Wekker, B. J. Snyder (Eds.), *Mountain weather research and forecasting: Recent progress and current challenges* (pp. 35–119). Netherlands: Dordrecht: Springer. https://doi.org/10.1007/978-94-007-4098-3_2

Zobel, D. B., McKee, A., Hawk, G. M., & Dyrness, C. T. (1976). Relationships of environment to composition, structure, and diversity of forest communities of the central western Cascades of Oregon. *Ecological Monographs*, *46*(2), 135–156. https://doi.org/10.2307/1942248

Journal of Geophysical Research: Atmospheres

Supporting Information for

Temperature Gradients and Inversions in a Forested Cascade Range Basin: Synoptic- to Local-Scale Controls

David E. Rupp[1], Sarah L. Shafer[2], Christopher Daly[3], Julia A. Jones[4], Sarah J. K. Frey[4]

[1]Oregon Climate Change Research Institute, College of Earth, Ocean, and Atmospheric Sciences, Oregon State University, Corvallis, OR, USA, [2]U.S. Geological Survey, Corvallis, OR, USA, [3]Department of Chemical, Biological, and Environmental Engineering, Oregon State University, Corvallis, OR, USA, [4]College of Earth, Ocean, and Atmospheric Sciences, Oregon State University, Corvallis, OR, USA

Contents of this file

Introduction

In this supporting information file, we provide examples of the adjustments made to temperature to reduce radiation-produced errors (section S1 and Figures S11 and S12) and provide additional details about how the cloud cover index was calculated (section S2). We also provide results of a boosted regression tree analysis using the same predictor variables as were used for the multivariate linear regression analysis described in the main text (section S3 and Figure S2). Additional figures (Figures S1 and S3-S10) and tables (Tables S1 to S3) supplement the analyses and results provided in the main text.

S1. Examples of the illumination-based temperature adjustment

Temperature measured along the transects was adjusted for radiation-produced temperature errors (see section 2.3.3). Here we show example time series of hourly temperature at the Upper Lookout Transect (ULT) during summer when the adjustment is largest. Figures S6 and S7 show the "raw" temperatures on the south- and north-facing sides of the transect, respectively, during a 72-hour period beginning 2 August 2012, 20:00 PST. Figures S11 and S12 show the adjusted temperatures on the south- and north-facing sides of the transect, respectively, during the same period. On the south-facing side, relative differences in sensor temperatures with (Figure S11) and without (Figure S6) the adjustment are small. On the north-facing side, the largest adjustments are the reduction in the late morning temperatures at sensor 518 and the

reduction in the mid- to late-afternoon temperature peak at sensor 520 (compare Figures S7 and S12).

S2. Cloud cover index and clear-sky insolation

The cloud cover index was calculated using observed insolation at VANMET as $Cc = (1 - X) / [1 - \min(X)]$, where X is the ratio of the observed daily insolation (Daly & McKee, 2019) to the estimated clear-sky insolation and $\min(X) = 0.01278$ is the minimum X over the entire period of record (2002-2018), such that Cc equals 0 for no clouds and equals 1 for $\min(X)$. The clear-sky insolation was estimated using the R "insol" package (Corripio, 2019) with the following parameters held constant: visibility = 30 km, relative humidity = 0%, temperature = 273.15 K, and surface albedo = 0. To improve the fit to the observed data without the complicating factor of compensating parameters, only one parameter was varied over the year: ozone thickness d (m), which was scaled up to serve as the optical depth due to effectively all contributing factors but clouds. Effective ozone thickness was varied over the year as $d = 20.5 - 0.3(\tau_i - \tau_0)$, where τ_i is the duration of daylight (hours) on day i of the year and τ_0 is the duration of daylight on December 23. The result is a higher effective optical depth in winter than summer, which in part substitutes for seasonally varying shading from topography and tall trees on nearby ridges, but also for seasonally varying mean values of the other parameters. The coefficients in the equation were determined by visually fitting an upper envelope to the long-term mean annual cycle of observed insolation at VANMET.

S3. Boosted regression trees

In contrast to multivariate linear regression, boosted regression trees do not assume a priori the functional form of the relationships, including interactions among predictor variables, but they are difficult to interpret and more susceptible to overfitting and spurious relationships (Elith et al., 2008). Boosted regression trees were fitted using the R "dismo" package with a bag fraction of 0.5, learn rate = 0.01, and a tree complexity of 3 (Hijmans et al., 2017).

S3.1 Nighttime air temperature inversions (06:00 PST)

Using boosted regression trees with the ERA5 free-air temperature gradient as a predictor, the factors explain as much as 75% of the variance at the basin-scale, and about 55% and 60% of the variance for the lower and upper transects, respectively (Figure S2a). The higher variance explained compared to multivariate linear regression reflects the relaxation of the linear assumption with the boosted regression trees. The free-air temperature is the most important factor, followed by vorticity, which is generally consistent with the multivariate linear regression results (Figure 9a). Cloudiness, flow strength, and daily clear-sky insolation all have low importance. The general lack of importance of cloudiness from the boosted regression trees relative to the linear regression is one notable discrepancy.

Removing the regional free-air temperature gradient from the boosted regression trees reduces the variance explained by 10 to 15% and leaves vorticity and cloudiness as the most important variables (Figure S2c), similar to the multivariate linear regression results (Figure 9c).

S3.2 Daytime air temperature inversions (14:00 PST)

Using boosted regression trees with the ERA5 free-air temperature gradient as a predictor, the factors explain as much as 75% of the variance at the basin-scale, and about 60% and 65% of the

variance for the lower and upper transects, respectively (Figure S2b). The free-air temperature gradient is the most important factor followed by clear-sky insolation everywhere but for the upper transect, where vorticity is the most important factor, which is generally consistent with the multivariate linear regression results (Figure 9b). Cloudiness is the third most important factor except at RS04-RS02, where it is fourth most important.

Removing the free-air temperature gradient from the boosted regression trees reduces the variance explained by about 10% and leaves clear-sky insolation as the most important variable (Figure S2d) except for at the upper transect where vorticity ranks highest, similar to the multivariate linear regression results (Figure 9d). Cloudiness and vorticity alternate between second and third most important variables across the datasets.

Disclaimer

Any use of trade, firm, or product names is for descriptive purposes only and does not imply endorsement by the U.S. Government.

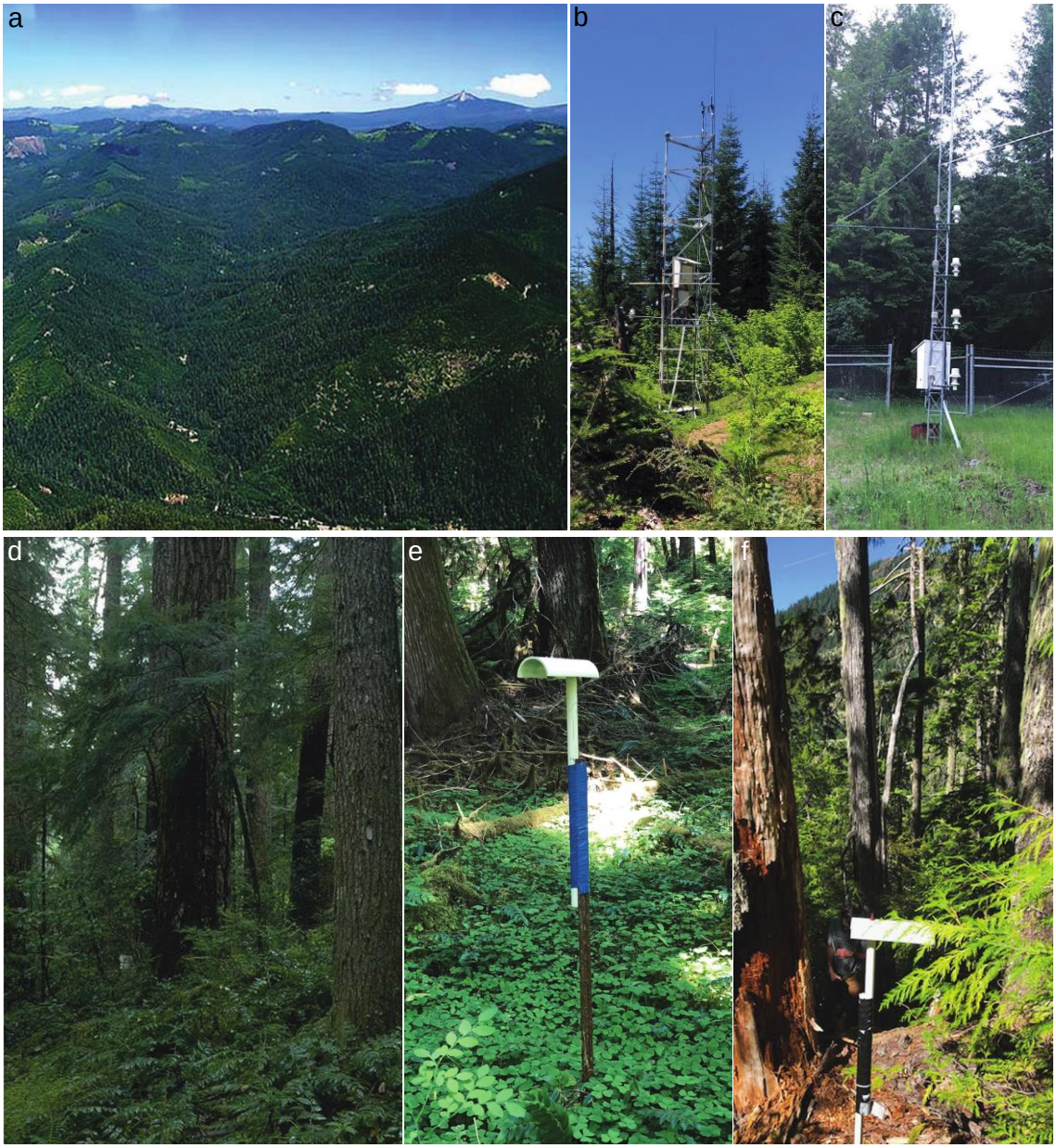

Figure S1. (**a**) Looking east up the Lookout Creek drainage basin (12 July 2005). (**b**) VANMET meteorological station (4 June 2019, 12:45 PDT). (**c**) PRIMET meteorological station (4 June 2019, 18:02 PDT). (**d**) Reference Stand 2 (RS02; April 1994). (**e**) Lower transect air temperature sensor site 504 (17 July 2018, 11:20 PDT). (**f**) Upper transect air temperature sensor site 520 (4 June 2019, 16:29 PDT). In (**e**) and (**f**), the temperature and illumination sensors are located under the white, horizontal PVC radiation shield. Photo credits: Andrews Forest LTER (**a**, CD AEA-020; **d**, CD AAQ-076) by A. Levno via Creative Commons licensing CC-BY; C. Daly (**b**, **c**, **e**, **f**)

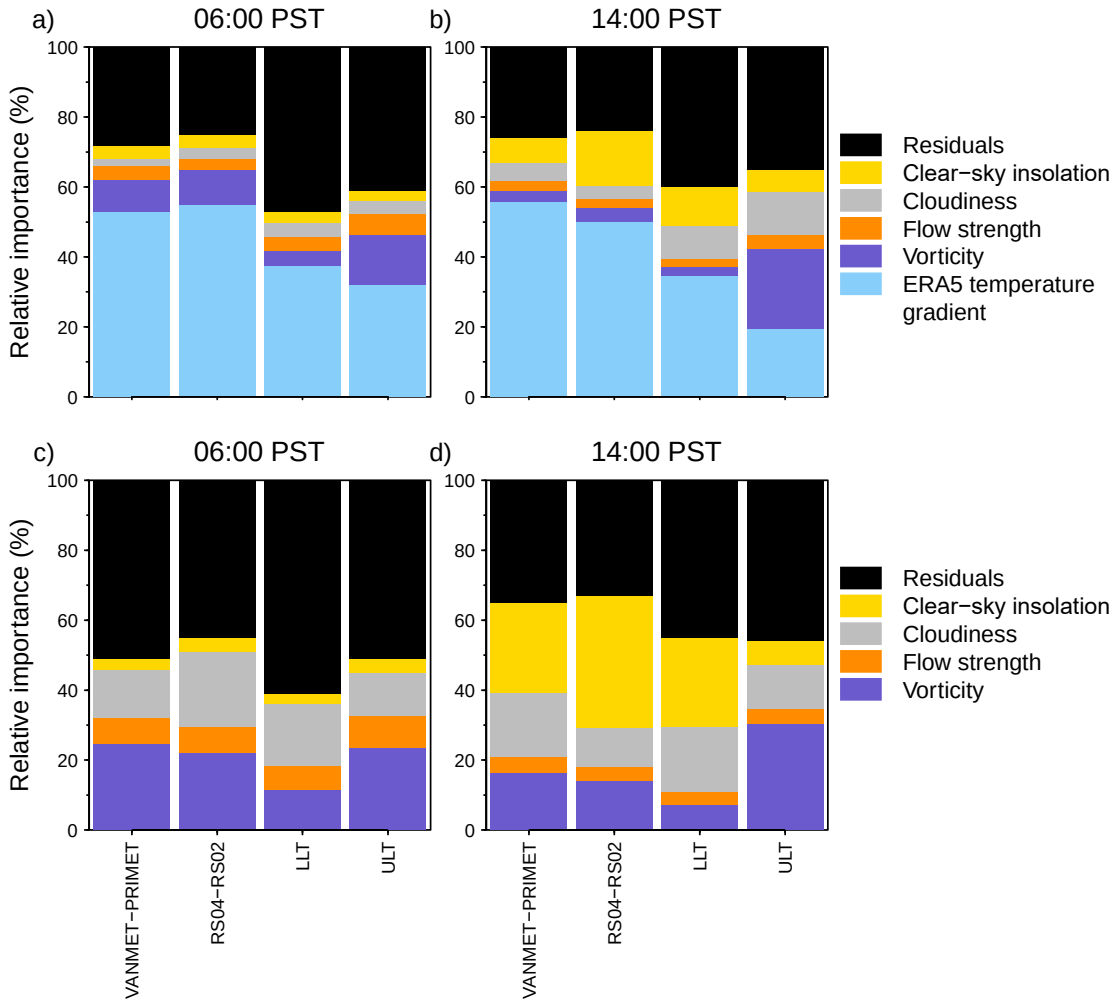

Figure S2. Relative importance of environmental predictor variables using boosted regression trees for predicting the magnitude of temperature gradients at the basin scale (VANMET-PRIMET, RS04-RS02) and the cross-valley lower transect (LLT) and upper transect (ULT) scale at (**a**, **c**) 06:00 PST (nighttime) and (**b**, **d**) 14:00 PST (daytime). Gradients at RS04-RS02, LLT, and ULT are based on temperature under the forest canopy, whereas gradients at VANMET-PRIMET are based on temperature in canopy openings. Gradients at LLT are in a wide valley (~2 km), whereas those at ULT are in a narrow valley (~1 km). The ERA5 temperature gradient was included as a predictor variable for the models in (**a**) and (**b**) but excluded from the models in (**c**) and (**d**).

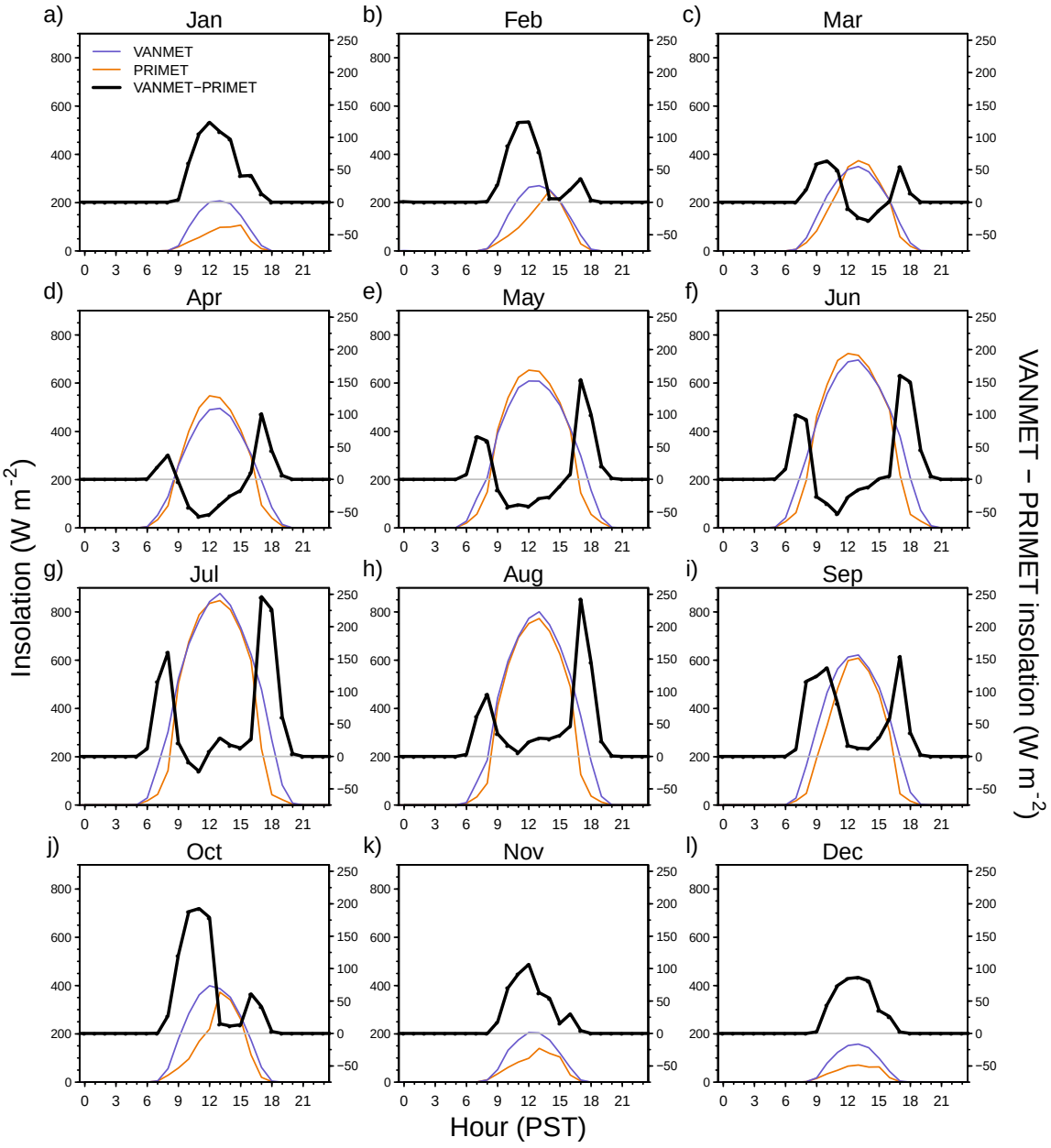

Figure S3. Mean insolation at PRIMET (red line) and VANMET (blue line) meteorological stations (left y-axis) and mean insolation at VANMET minus mean insolation at PRIMET (black line; right y-axis) by calendar month and hour of day for the years 2006-2018.

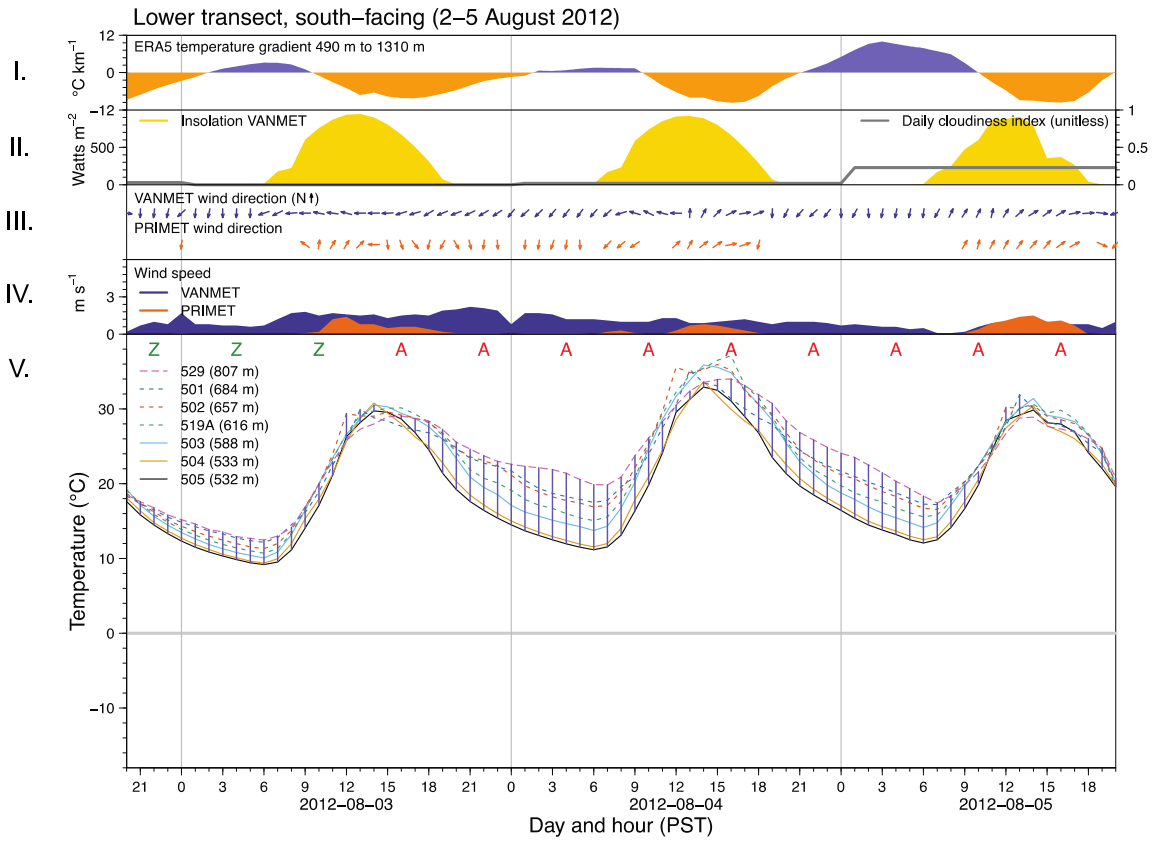

Figure S4. Time series of environmental variables and hourly temperature at the south-facing lower transect from 2 August 2012, 20:00 PST, to 5 August 2012, 20:00 PST. This figure is a single image from animations spanning July 2002 through December 2018 (Rupp et al., 2020). The data displayed in the six figure panels are:

I. ERA5 hourly temperature gradient between 490 and 1310 m ~65 km west of Andrews Forest. Positive (negative) gradients are shaded in purple (orange).

II. Hourly insolation (yellow shading) and daily cloudiness index (gray line) at VANMET.

III. Hourly wind direction (north = up) at VANMET (purple) and PRIMET (orange). Missing arrows indicate wind speeds <0.1 m s^{-1}.

IV. Hourly wind speed (m s^{-1}) at VANMET (purple) and PRIMET (orange).

V. Hourly temperature at the south-facing lower transect. Vertical purple lines show the presence of inversions from the lowest sensor on the transect (sensor 505) to the highest sensor on the transect that is also warmer than sensor 505. Letters at the top of the panel give the 6-hourly synoptic-scale flow pattern: “A” = anti-cyclonic, “Z” = zonal, “C” = cyclonic. Note that temperature data displayed are observations before adjustment for radiation-produced temperature errors (see section 2.3.3). The vertical gray lines indicate midnight.

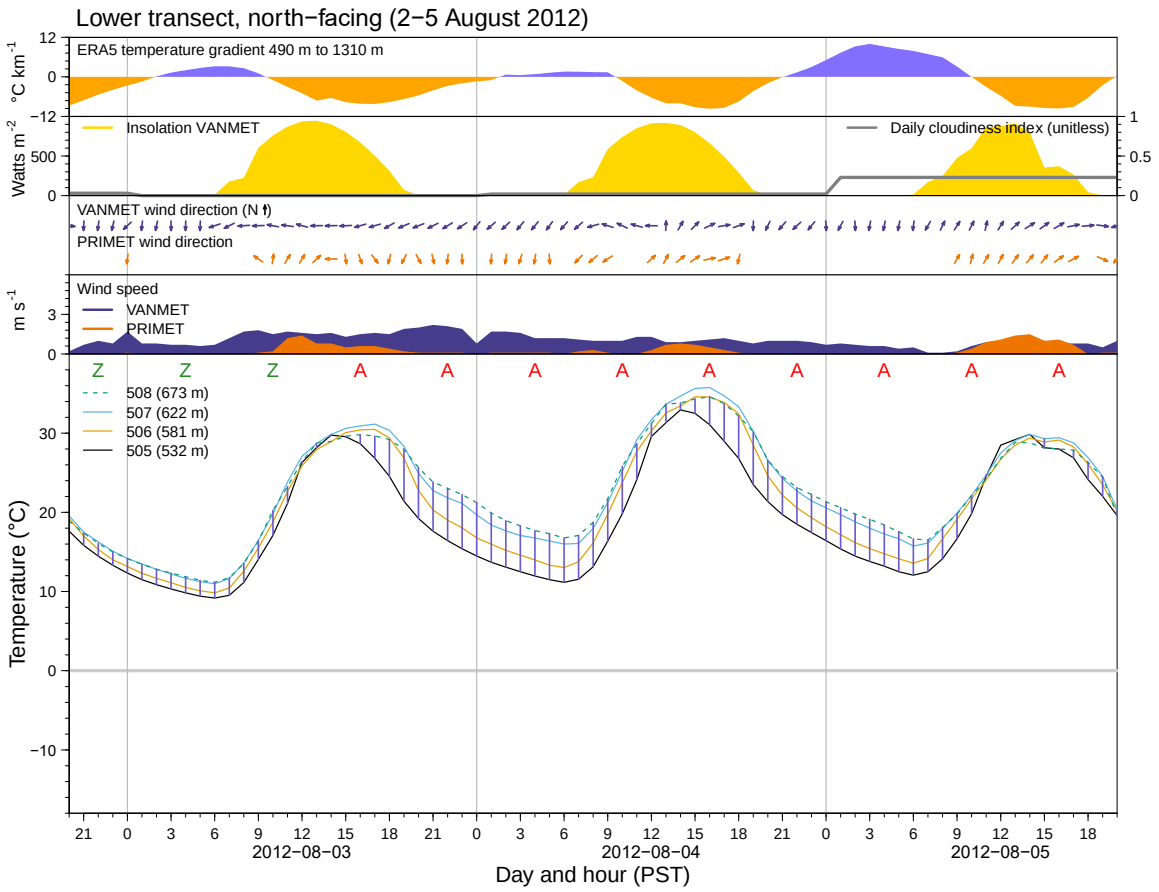

Figure S5. Same as Figure S4 but for the north-facing lower transect from 2 August 2012, 20:00 PST, to 5 August 2012, 20:00 PST.

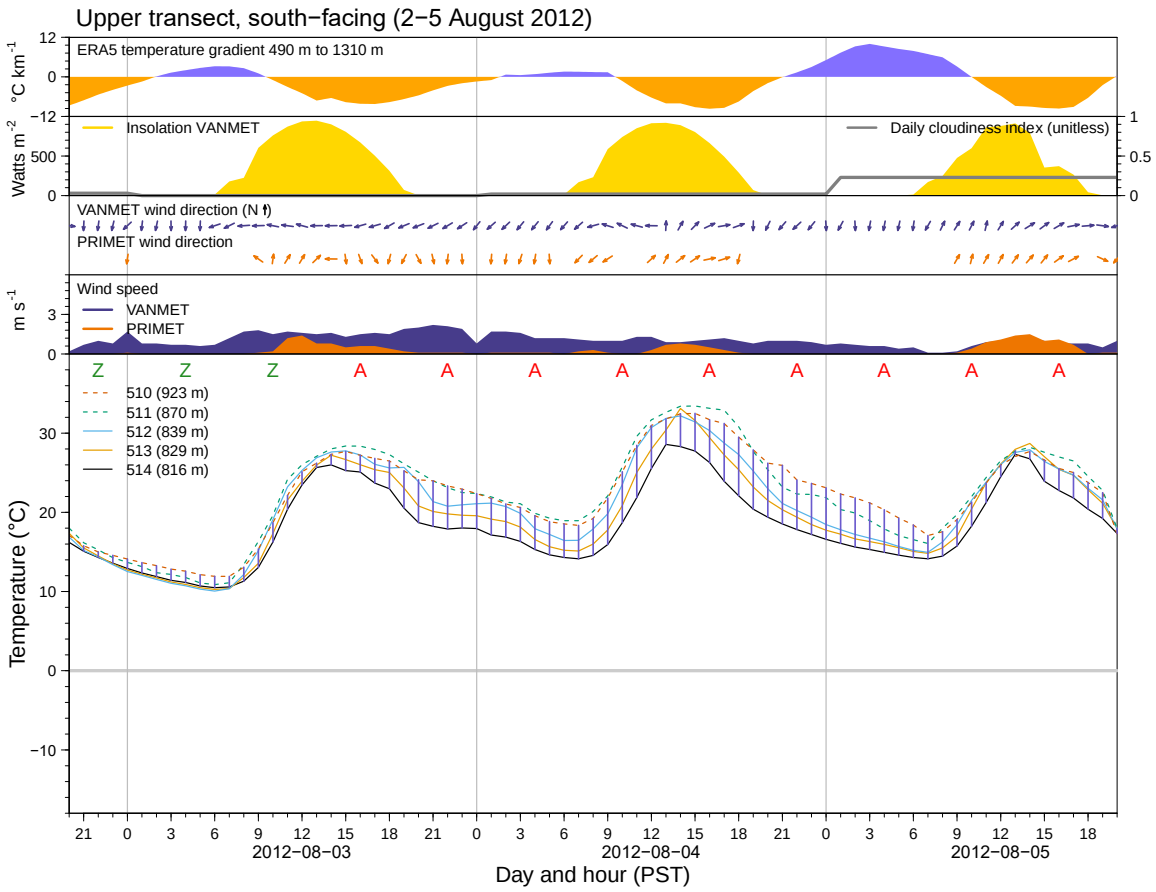

Figure S6. Same as Figure S4 but for the south-facing upper transect from 2 August 2012, 20:00 PST, to 5 August 2012, 20:00 PST.

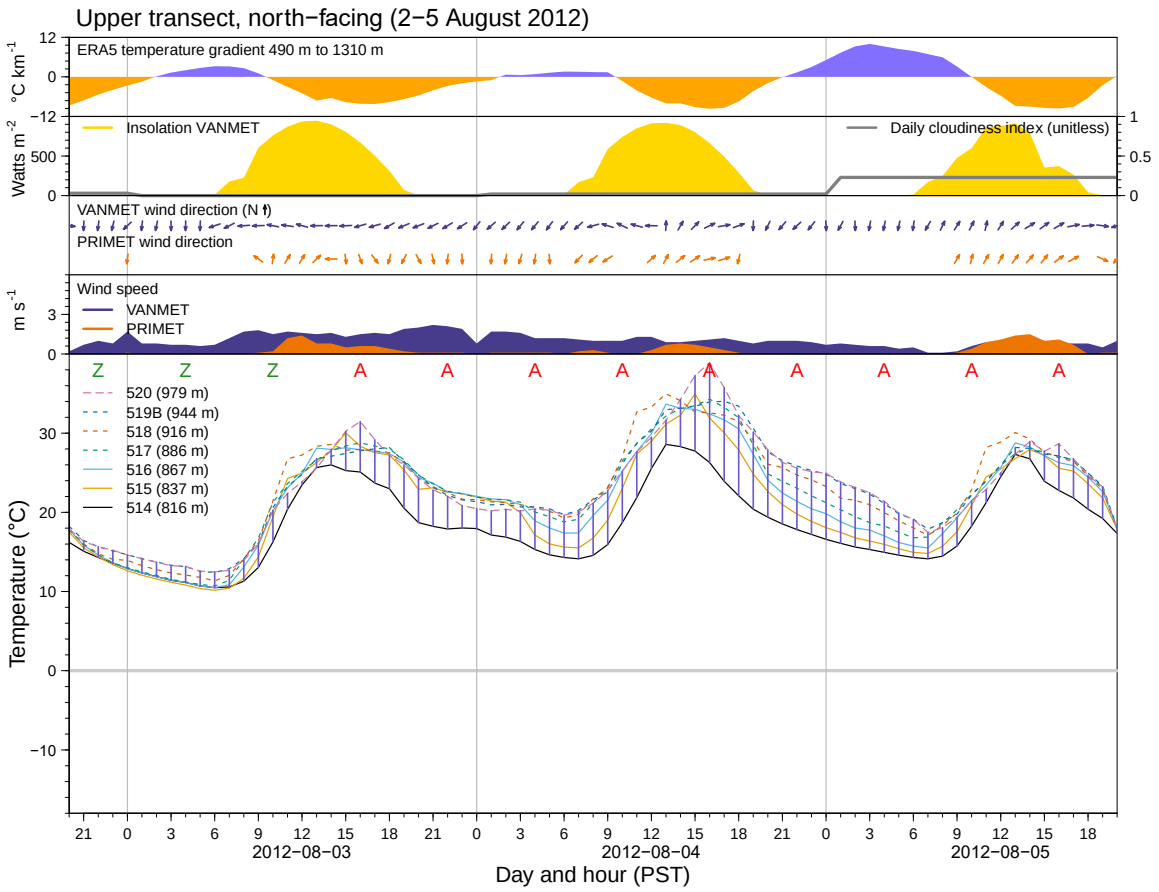

Figure S7. Same as Figure S4 but for the north-facing upper transect from 2 August 2012, 20:00 PST, to 5 August 2012, 20:00 PST.

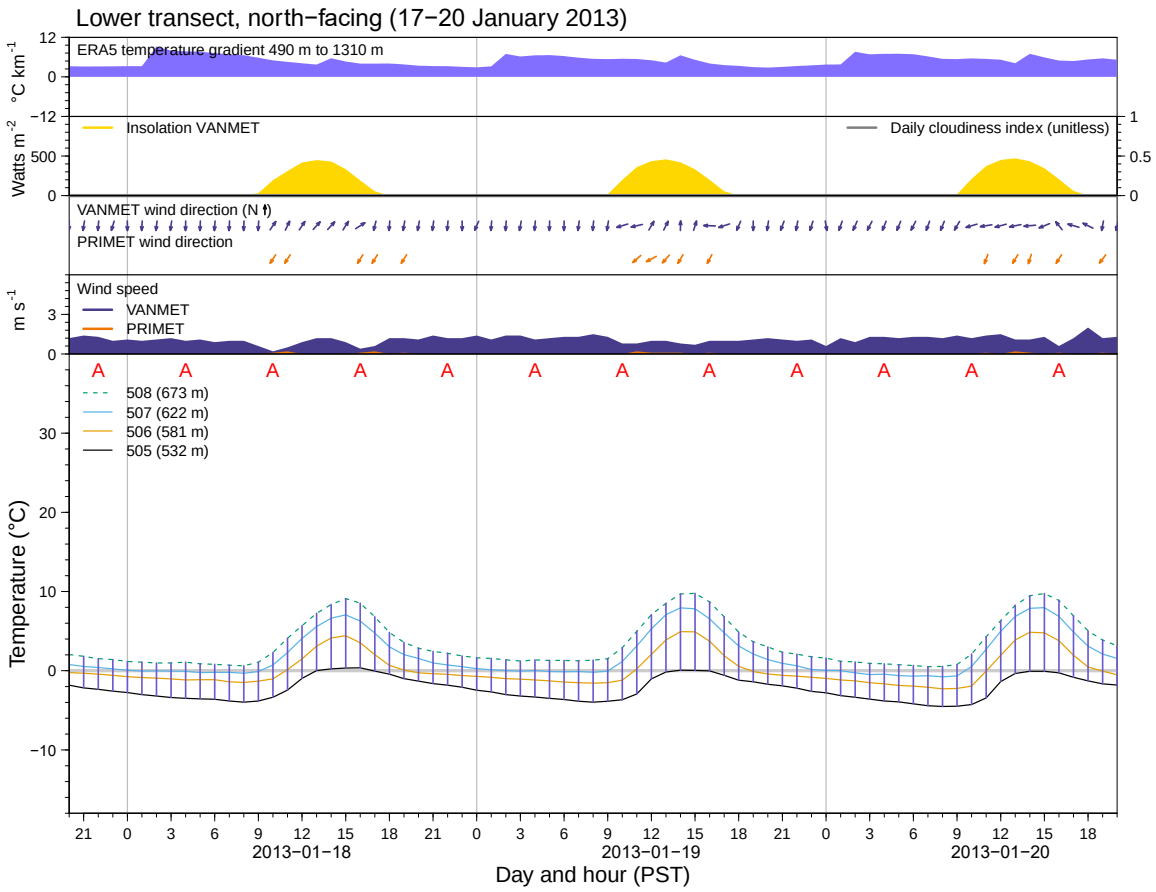

Figure S8. Same as Figure S4 but for the north-facing lower transect from 17 January 2013, 20:00 PST, to 20 January 2013, 20:00 PST. Data for the south-facing lower transect for the same time period are shown in Figure 12c.

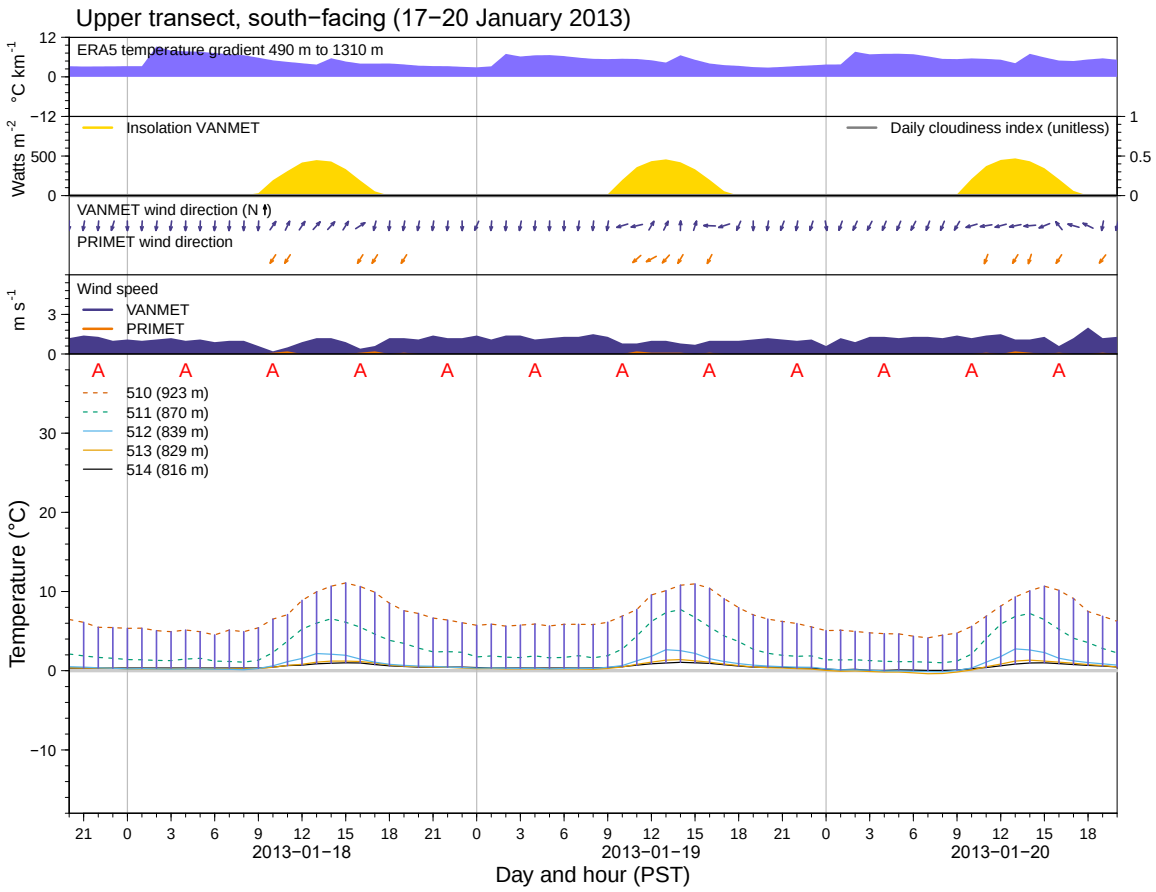

Figure S9. Same as Figure S4 but for the south-facing upper transect from 17 January 2013, 20:00 PST, to 20 January 2013, 20:00 PST.

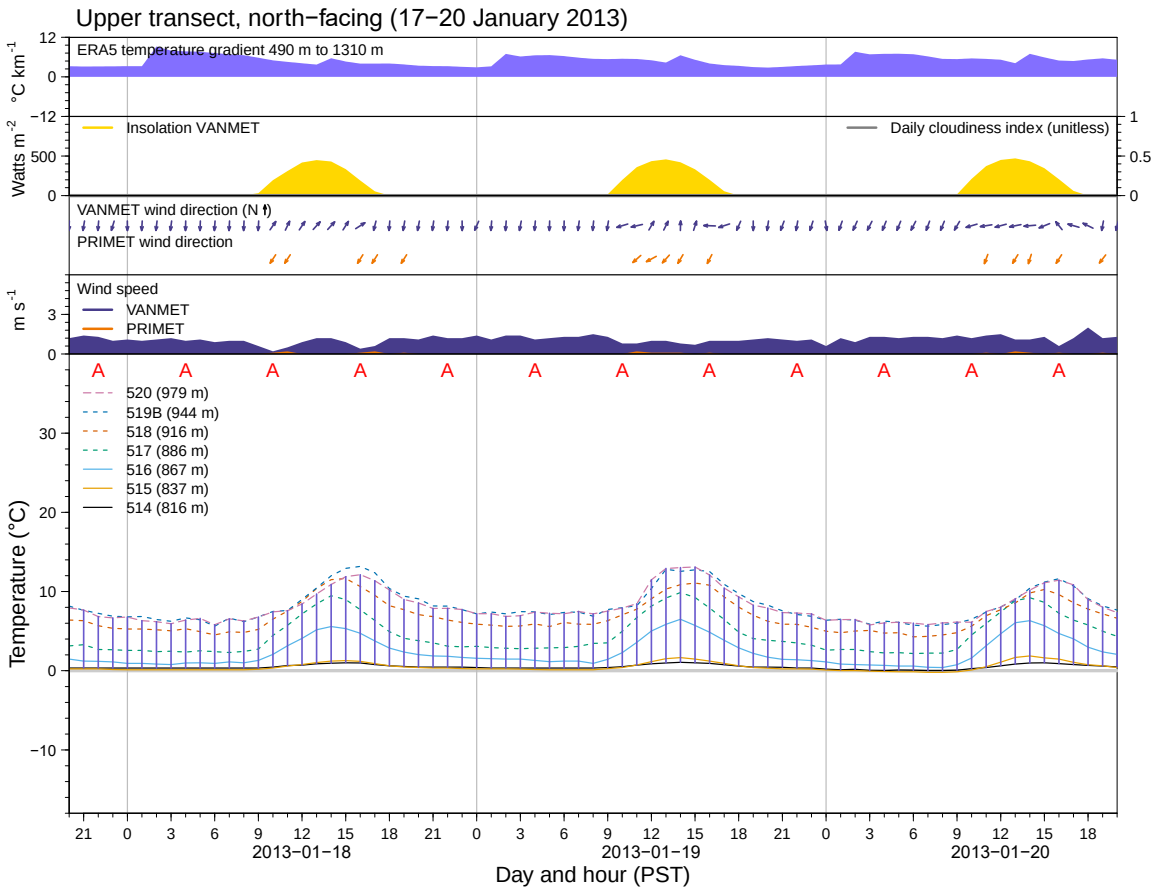

Figure S10. Same as Figure S4 but for the north-facing upper transect from 17 January 2013, 20:00 PST, to 20 January 2013, 20:00 PST.

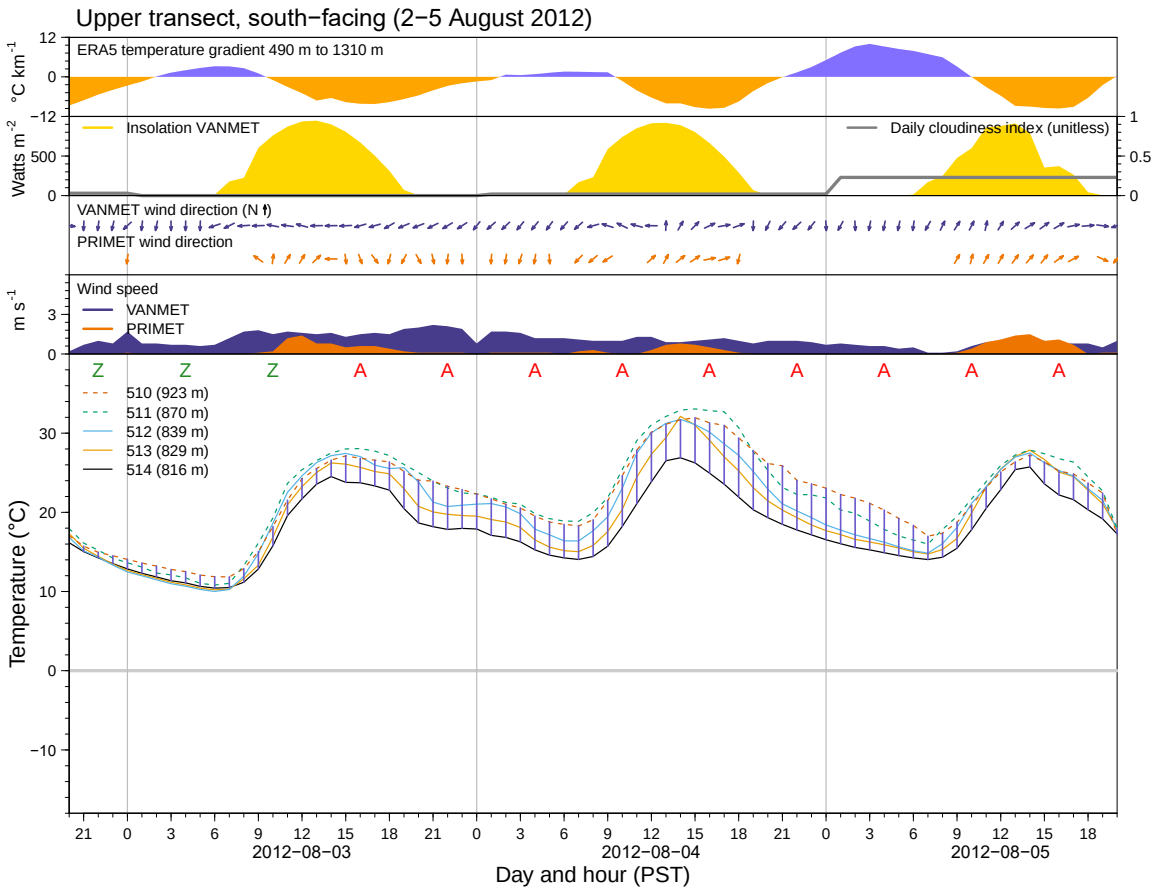

Figure S11. Same as Figure S6 but after the temperature adjustment to account for illumination effects (section 2.3.3). Relative differences in sensor temperatures with and without (Figure S5) the adjustment are small.

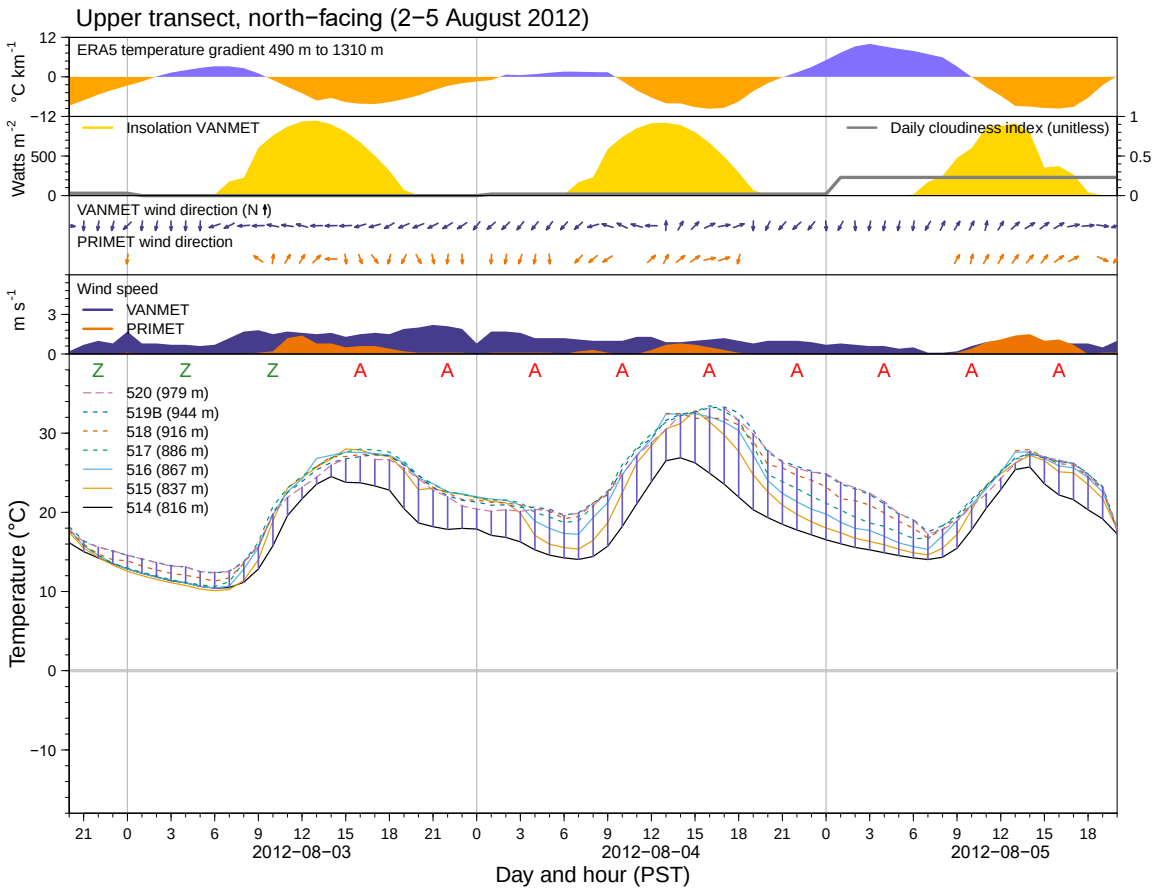

Figure S12. Same as Figure S7 but after the temperature adjustment to account for illumination effects (section 2.3.3). The largest adjustments are the reduction in the late morning temperatures at sensor 518 and the reduction in the mid- to late-afternoon peak at sensor 520.

Table S1. *Automated Quality Control (QC) Flagging Criteria for Lower and Upper Transect Data at 15-Minute Intervals*

Flag type	Criteria
Extreme temperature	Temperature <-20.7 °C or >42 °C
Spike in temperature	7 °C deviation from centered 7-record median
High light intensity	Intensity >20,000 lux
Possible snow burial of sensor	Temperature >-0.7 °C and <0.7 °C for ≥48 hours

Table S2. *Coefficients of Multivariate Linear Regression of Temperature Gradients Against Environmental Variables at 06:00 and 14:00 PST*

Time (PST)	Dataset	ERA5[a] [°C km^{-1} °C^{-1} km]	Vorticity [°C km^{-1} m^{-1}]	Flow strength [°C km^{-1} m^{-1}]	Cloudiness[b] [°C km^{-1}]	Solar[c] [°C km^{-1} MJ^{-1} m^2 day]
06:00	VANMET-PRIMET	**0.73**	**-0.0051**	0.0088	**-0.81**	-0.061
	RS04-RS02	**0.75**	**-0.0065**	0.0048	**-1.44**	-0.053
	LLT[d]	**0.96**	**-0.0075**	0.0221	**-5.35**	-0.032
	ULT[e]	**1.32**	**-0.0413**	0.0144	**-5.25**	-0.004
14:00	VANMET-PRIMET	**0.75**	**-0.0001**	0.0068	-3.47	**-0.104**
	RS04-RS02	**0.56**	-0.0005	0.0021	-1.00	**-0.135**
	LLT	**1.02**	-0.0047	0.0082	-8.38	**-0.413**
	ULT	**1.52**	**-0.0370**	0.0224	**-16.59**	0.009
06:00	VANMET-PRIMET	-	**-0.0141**	-0.0054	**-4.24**	-0.085
	RS04-RS02	-	**-0.0151**	-0.0085	**-4.81**	-0.059
	LLT	-	**-0.0227**	-0.0069	**-11.19**	-0.123
	ULT	-	**-0.0547**	-0.0079	**-11.27**	0.075
14:00	VANMET-PRIMET	-	**-0.0065**	0.0007	**-4.04**	**-0.291**
	RS04-RS02	-	**-0.0053**	-0.0027	-1.49	**-0.267**
	LLT	-	**-0.0135**	-0.0015	-9.70	**-0.765**
	ULT	-	**-0.0499**	0.0114	**-17.91**	-0.393

Note. "ERA5" was excluded from the multivariate linear regression model for results presented in the bottom eight rows. Variables explaining ≥5% of the variance are in bold font. [a]ERA5 = ERA5 temperature gradient over same elevation range of each dataset. [b]Cloudiness = daily average cloudiness index: 0 = clear sky, 1 = maximum obscuration. [c]Solar = daily clear-sky solar radiation on a horizontal surface without hillshading. [d]LLT = lower transect. [e]ULT = upper transect.

Table S3. *Pearson Correlation Coefficients of Predictor Variables in Multivariate Linear Regression of RS02-RS04 Temperature Gradients Against Environmental Variables at 06:00 and 14:00 PST*

	Solar[a]	Cloudiness[b]	ERA5[c]	Vorticity	Flow strength
Solar	1	-0.35	-0.13	0.16	-0.43
Cloudiness		1	-0.33	0.42	0.54
ERA5			1	-0.38	-0.20
Vorticity				1	0.04
Flow strength					1

[a]Solar = daily clear-sky solar radiation on a horizontal surface without hillshading. [b]Cloudiness = daily average cloudiness index: 0 = clear sky, 1 = maximum obscuration. [c]ERA5 = ERA5 temperature gradient over same elevation range as the RS04-RS02 sensors.